An experimental study on pre-stretched double-chamber 6000-series aluminium profiles subjected to quasi-static and dynamic axial crushing

Kristin Qvale [a,*], Odd Sture Hopperstad [a,b], Oddvin Reiso [c], Ulf Håkon Tundal [c], Calin Daniel Marioara [d], Tore Børvik [a,b]

[a] Structural Impact Laboratory (SIMLab), Department of Structural Engineering, Norwegian University of Science and Technology (NTNU), NO-7491, Trondheim, Norway
[b] Centre for Advanced Structural Analysis (CASA), NTNU, Trondheim, NO-7491, Norway
[c] Hydro Aluminium Research and Technology Development Sunndal, Sunndalsøra, NO-6600, Norway
[d] Materials and Nanotechnology, SINTEF Industry, Trondheim, NO-7465, Norway

ARTICLE INFO

ABSTRACT

Automotive crash boxes require a material selection with strength and ductility in a balanced combination. In this work, the behaviour of double-chamber AA6063 and AA6082 aluminium profiles subjected to quasi-static and dynamic axial crushing was studied experimentally. The profiles were stretched to two different levels between extrusion and artificial ageing to temper T6. The higher pre-stretch resulted in a more ductile material with a slightly lower ultimate tensile strength. By visual inspection and by studying X-ray Computed Tomography scans of the tested profiles, dynamic loading was found to cause a larger amount of fracture than quasi-static loading.

1. Introduction

Due to a high strength-to-weight ratio combined with high ductility, aluminium alloy components have good specific energy absorption capacity and are often used in energy absorbing structures that require low weight. With an ever increasing focus on safety and fuel efficiency of cars, lightweight energy-absorbing components are particularly relevant in the automotive industry. Crash boxes are an example of such components, often constructed from thin-walled extruded profiles, designed to absorb impact energy through progressive buckling of the profile walls. For optimal energy absorption, material failure should be avoided. Fracture and energy absorption are closely coupled, as fracture may alter the deformation mode and hence the energy dissipated in material deformation [1,2]. However, some studies report that incipient fracture has no detectable effect on the global response nor the energy absorption of thin-walled profiles [3,4].

The 6000-series aluminium alloys normally have a low strain-rate sensitivity at room temperature [5]. However, inertia effects coupled with the material properties may cause the response of components to impact loading to differ considerably from the quasi-static response [3, 6]. Typical differences between quasi-static and dynamic loading seen in axial crushing include increased mean and initial peak force as well as an altered folding pattern for the latter [3,6,7]. Small imperfections in the profiles play a more significant role under impact loading than under quasi-static loading. To mitigate the unfavourable behaviour as a result of these, a preferred deformation mode can be purposefully triggered by imposing an appropriate imperfection to the profile. When Langseth and Hopperstad [3] introduced static pre-buckling on their profiles, they found that the subsequent dynamic folding pattern matched the quasi-static tests. Also, although not reduced to the same level as in the quasi-static tests, the particularly high initial forces of the dynamic tests were reduced such that the force level was stably above the quasi-static level throughout the displacement history. Zhang et al. [7] installed a pre-hit column on the profile, which was hit by the impactor before the profile was reached. Upon impact, the pre-hit column pulled the walls of the profile, acting as a pre-buckling device. As the impactor further reached the profile, the profile had achieved an imperfection triggering the progressive buckling pattern. This method also showed to significantly reduce the initial peak force and prevent any irregularities in the folding pattern. Other ways of ensuring a stable progressive buckling pattern include thermally induced triggers [8], i.e., a local softening of the material by a local heat treatment, and geometrical triggers on the

---

impacting end [4,9]. The latter is used in this study.

Analytical and numerical studies done on the crushing of multi-cell profiles show an increased specific energy absorption compared to single-cell aluminium profiles [10,11]. Zhang et al. [11] derived analytical expressions for finding the theoretical mean force of the various sections in multi-square-cell profiles, i.e., the criss-cross part, the T-junction and the corner part, using the approach proposed by Chen and Wierzbicki [10]. Zhang et al. [11] found that the criss-cross part and the T-junction both absorb more energy per unit mass compared to the corner part, and that a 3-by-3-cell profile may absorb 50% more energy than a single-cell profile of the same mass. Similar geometries to the one used in this study, i.e., double-chamber profiles with large-radius corners, have previously been studied experimentally under quasi-static and dynamic loading [9,12]. It is clear from these studies that the T-junction is particularly prone to fracture and that the damage increases for dynamic loading. Gu et al. [2] showed by numerical studies that fracture is most likely to occur in the corners of square profiles, with the probability increasing as the wall thickness and the sharpness of the corners increase. Additionally, the corner area has been found to be an important prospect for design in the optimization of the energy absorption of square profiles [13]. Since the probability of fracture is higher in areas where the potential for increased energy absorption is higher, an accurate prediction of failure is essential for numerical studies in design of profiles for optimized energy absorption.

Aluminium profiles need to be straightened after extrusion, as the high cooling rates after exiting the extrusion press, together with uneven flow velocity in the profile during extrusion, cause the profiles to warp [14]. The industrial standard for extruding 6000-series aluminium alloys is to stretch the profiles to between 0.3 and 1.0% plastic strain. This straightening process with subsequent artificial ageing has a complex effect on the microstructure. The pre-stretching generates dislocations, which become heterogeneous nucleation sites for precipitates during the subsequent ageing. The overall effect in this case is a coarsening of the microstructure with fewer, larger precipitates at peak hardness compared to the undeformed conditions. The strengthening contribution from precipitates becomes lower, but the pre-stretched conditions can have comparable or higher hardness than the undeformed ones due to the added contribution from dislocations [15]. Due to the faster solute and vacancy transport caused by the increased dislocation density, the precipitation kinetics is accelerated [15].

The literature covering the effect on the resulting mechanical properties from pre-stretching is limited, and to the authors' knowledge, the effect on ductility has yet not been considered. Kolar et al. [16] studied an AA6060 alloy subjected to various extents of pre-stretching between 0 and 10% and subsequent artificial ageing at 190 °C for between 10 and 300 min. Their results showed that the yield and ultimate tensile strength were improved for increased pre-stretching, with the largest effect for the shorter ageing times and only a small effect when aged for 300 min. Furu et al. [17] observed reduced elongation to necking in alloys AA6060, AA6005 and AA6082 aged to peak strength, while the yield strength, work hardening and post-necking elongation were not affected by pre-stretching in the range of 0 to 5 or 10%. There were, however, significant effects in underaged materials, with increased yield and tensile strengths.

In this study, the crushing behaviour of AA6063 and AA6082 double-chamber profiles that, after extrusion, have been stretched to the required minimum plastic strain for straightening, is compared to the behaviour of profiles that have been stretched significantly more. After stretching, all profiles have been artificially aged to temper T6. The profiles are tested both quasi-statically and under impact conditions, and have subsequently been CT scanned to enable a thorough study of fracture in the profiles. A TEM study has also been carried out to find out how the stretching affects the materials at the nano-scale. The main objectives of this study are: (1) to investigate the effects of the pre-stretching on the mechanical properties, the microstructure and the crushing response; (2) to study the difference between the response of the profiles to quasi-static and dynamic loading; (3) to provide an experimental database for validation of a novel microstructure-based modelling framework currently being developed.

2. Materials and geometry

Extrusions of alloys AA6063 and AA6082 were studied. The chemical compositions of the alloys are given in Table 1. A separate solution heat treatment of 6000-series alloys extruded at high temperatures has been found to have little effect on the final precipitation heat treatment [18], and the extrusions were hence not separately solutionized. However, the T6 designation is still used, as this is common practice. After extrusion and water quenching, the extrusions of each material were stretched to 0.5% or 4% plastic strain, before heat treatment to temper T6. The T6 temper was achieved by artificial ageing for 6 h at 185 °C of the AA6063-profiles and 8 h at 170 °C of the AA6082-profiles, i.e., there was no distinction in the ageing times between the levels of pre-stretching. After these times at elevated temperatures, the oven was turned off and the door opened, and the profiles were left to cool down to room temperature. It is noted that the profiles were stored at room temperature for around 10 months between stretching and heat treatment.

The profiles' nominal cross-sectional geometry is shown in Fig. 1. The seam welds are located at the four corners and on the inner wall, as indicated in the figure. The water spray that cools the profile as it exits the press does not reach the inner wall, and the effective cooling rate of the inner and outer walls is hence different. This is expected to have an impact on the tensile behaviour of the material, such as found in Ref. [19], where there were significant differences in the mechanical properties between an air-cooled and a water-quenched AA6060 alloy. Flat tensile test specimens with geometry as shown in Fig. 2 were cut by wire erosion from both the inner and the outer wall according to the indications in Fig. 1 along the extrusion direction.

Fig. 3 shows images of the grain structure of material taken from the inner walls and the side walls of the extrusions, i.e., the same location as the tensile test specimen extraction. Samples were cut out of the profiles and moulded in epoxy, then ground with SiC paper and polished using polishing pads. Subsequently, the samples were electropolished and anodised before the grain structure images were taken using polarized light in an optical microscope. Fig. 3 shows that AA6063 is recrystallized and that AA6082 is non-recrystallized in the centre, but with a wide layer at the surface that is recrystallized with large grains. No differences were seen for the grain structure between the two levels of pre-stretching for either of the alloys. In AA6082, it is noted that the inner wall has a wider recrystallized layer compared to the outer wall. This could be caused by the slower cooling of the inner wall or differences in the material flow in the profile during extrusion. Additionally, some larger grains have formed within the non-recrystallized layer, which can be seen in Fig. 3f.

3. Tensile tests

3.1. Test set-up

The tensile tests were performed in an Instron 5900 series universal testing machine equipped with a 30 kN load cell. As the strain-rate sensitivity of 6000-series aluminium alloys has previously been shown to be low [5], only quasi-static tests were conducted. A set of three repetitions was run for each material configuration. The specimens were loaded at a constant cross-head velocity of 2.1 mm/min, corresponding

Table 1
Chemical composition of alloys AA6063 and AA6082 (in wt%).

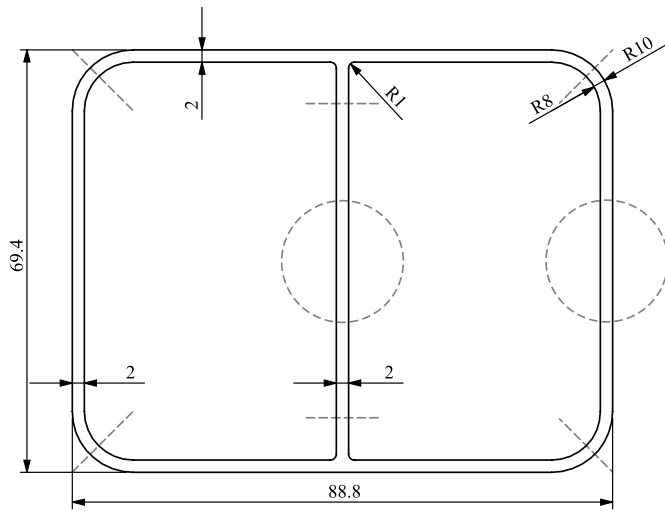| Alloy	Fe	Mn	Mg	Si	Cr	Ti	Al
AA6063	0.22	0.05	0.48	0.54	<0.01	0.01	Remainder
AA6082	0.17	0.53	0.65	0.93	<0.01	0.02	Remainder

Fig. 1. Nominal cross-sectional geometry of the profiles. Dimensions are in mm. The grey dashed circles indicate where on the cross section the tensile test specimens were taken from. The grey dashed lines show the locations of the seam welds.
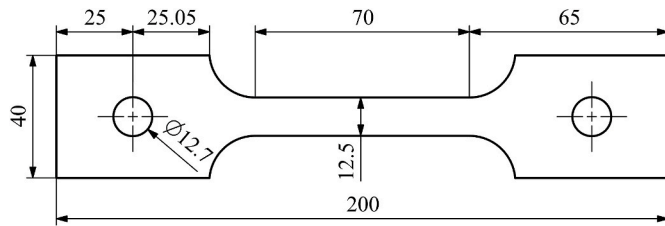

Fig. 2. Geometry of the tensile test specimen. Dimensions are in mm. The thickness is equal to the wall thickness of the extrusion.

to a constant engineering strain rate of the gauge region of $5 \cdot 10^{-4}$ s^{-1}. A lamp was placed to light up the specimen, while one Prosilica GC2450 camera was capturing the deformation of the specimen at 2 Hz with a

resolution of 2448×830 pixels. The specimens, with geometry presented in Section 2, were painted with a black-and-white speckle pattern before testing to prepare for post-processing with digital image correlation (DIC).

3.2. Results

2D finite-element-based DIC was performed on the photo series from each test using the in-house DIC software eCorr version 4.1 [20]. A Q4-element mesh covering the entire gauge region was placed on the first frame in each photo series. The mesh had 11 square elements across the width, corresponding to an element size of approximately 25×25 pixels or 1.1 mm $\times$ 1.1 mm. The engineering strain was then measured by the elongation of an initially 40 mm long vector placed on the first frame, making sure it covered the area where the neck and the fracture would occur in later frames, working as a virtual extensometer. The resulting engineering stress–strain curves are shown in Fig. 4, and values for the yield stress, the tensile strength and the logarithmic strain at necking can be found in Table 2. The 0.2% proof stress was found as the engineering stress at 0.2% plastic strain. The ultimate tensile strength (UTS) was defined as the maximum point on the engineering stress–strain curve. The logarithmic strain at necking was calculated as $\varepsilon_l = \ln(1 + e)$ at the same point, where e is the engineering strain. Since these are flat tensile test specimens and the equivalent stress and strain consequently cannot be calculated for the entirety of the test, the ductility cannot be disclosed directly from these data, but will be covered in the next section. One may, however, obtain a good indication of the trends in ductility by comparing the drop in stress from UTS to failure on the engineering stress–strain curves, since a larger drop indicates a greater reduction in cross-sectional area and hence larger local strains. Fig. 4 hence indicates that higher pre-stretch causes a more ductile material and that AA6063 is more ductile than AA6082, despite the engineering strain being higher at failure for the latter.

When comparing AA6082 to AA6063, higher yield and tensile strengths are seen for AA6082. Higher yield and tensile strengths are also seen for 0.5% pre-stretch compared to 4% pre-stretch for both alloys, except for the yield stress of the AA6082 alloy, which for 4% pre-stretch is higher than for 0.5%. With the exception of the yield stress of the 0.5% pre-stretched AA6082 alloy, the general trend throughout the
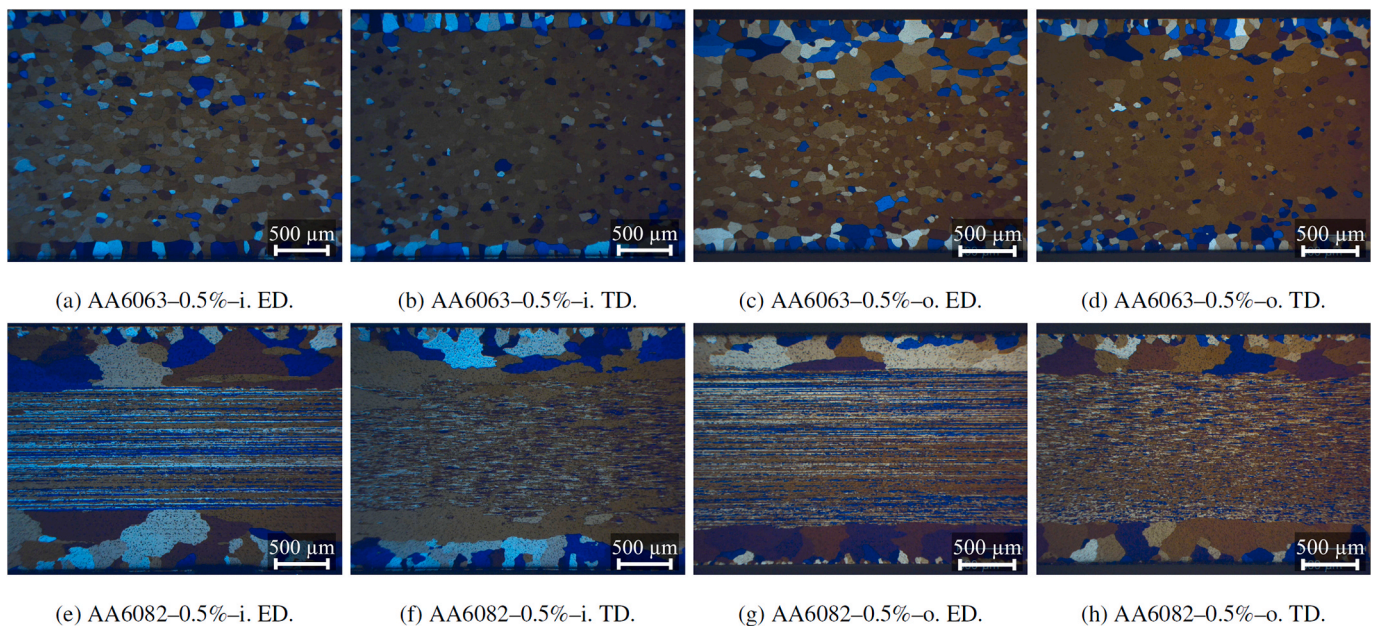

(a) AA6063–0.5%–i. ED.

(b) AA6063–0.5%–i. TD.

(c) AA6063–0.5%–o. ED.

(d) AA6063–0.5%–o. TD.

(e) AA6082–0.5%–i. ED.

(f) AA6082–0.5%–i. TD.

(g) AA6082–0.5%–o. ED.

(h) AA6082–0.5%–o. TD.

Fig. 3. Grain structure of the studied alloys. The designation AA60xx–y%–z represents the alloy number, the pre-stretch, and the wall from which the material is taken from by xx, y and z, respectively. i = inner wall, o = outer wall. ED = extrusion direction, TD = transverse direction.
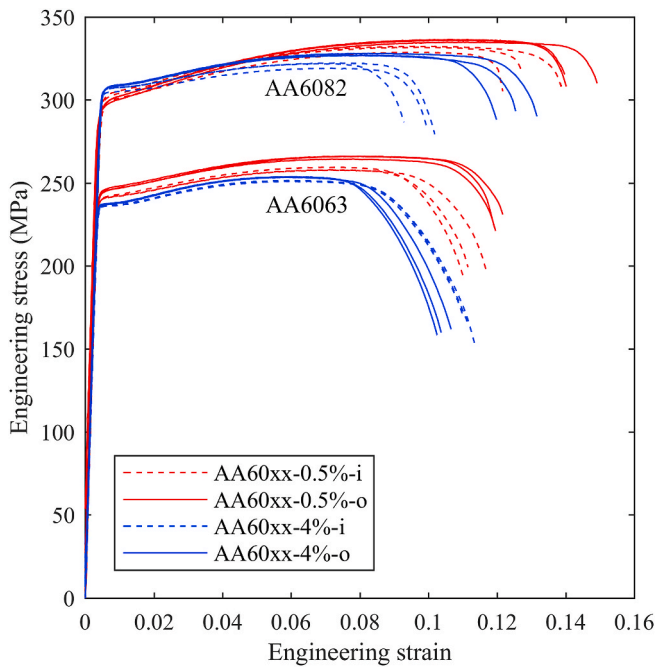
Fig. 4. Engineering stress–strain curves from the tensile tests plotted to fracture. The legends follow the same designation as in Fig. 3.

Table 2
Values for 0.2% proof stress and ultimate tensile strength, as well as the logarithmic strain at necking, for all the tensile tests.

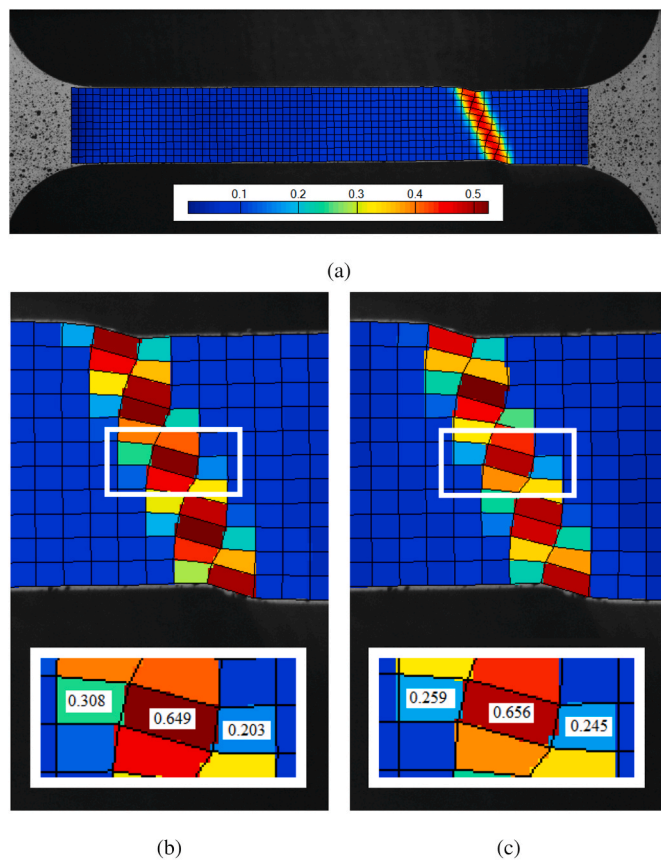| Alloy	Pre-stretch	Inner/outer wall (i/o)	0.2% proof stress (MPa)	Ultimate tensile strength (MPa)	Logarithmic strain at necking
AA6063	0.5%	i	240.7	258.0	0.069
			240.5	257.8	0.070
			241.3	259.5	0.067
		o	246.0	266.2	0.072
			245.2	264.5	0.075
			244.5	266.2	0.076
	4%	i	236.3	251.6	0.059
			236.1	251.3	0.059
			235.9	251.0	0.058
		o	236.8	253.6	0.058
			237.4	253.8	0.059
			237.0	253.5	0.055
AA6082	0.5%	i	301.1	331.7	0.092
			298.2	328.7	0.090
			302.7	332.3	0.097
		o	297.1	334.9	0.104
			298.6	335.9	0.101
			298.6	336.4	0.101
	4%	i	306.6	321.9	0.066
			304.4	319.1	0.069
			306.7	322.3	0.071
		o	307.1	326.8	0.078
			307.5	327.0	0.074
			307.4	328.1	0.079

precipitates and precipitate free zones. It can be observed in Table 2 that the logarithmic strain at necking is much higher for AA6082 than for AA6063, and for the 0.5% pre-stretched materials than for the corresponding 4% pre-stretched materials. Regarding the difference seen for the varying pre-stretches, it may be related to some of the potential for work hardening being consumed in the pre-stretching. Little difference is seen when comparing the strain at necking for the inner wall specimens and the outer wall specimens for AA6063, while the inner wall specimens of AA6082 has a lower strain at necking than the outer wall specimens. The strain at necking appears to be a repeatable measure throughout the test series.

It is observed in Fig. 4 that the higher pre-stretch causes a more distinct yield plateau on the stress–strain curves. This is also observed in Ref. [16] in the pre-stretched samples. A yield plateau is often associated with the occurrence of Lüders bands, which, however, is not a common occurrence in 6000-series alloys [21]. Lüders bands were hence searched for in the DIC analyses by studying the strain-rate fields, but no indications of them were seen.

3.3. Ductility

Several factors make determining the failure strain accurately in flat tensile tests difficult. As flat specimens often form a localized neck at an angle to the transverse direction, measuring the strain accurately after necking is not as straightforward as for cylindrical specimens, where the diameter reduction can be monitored. Additionally, measuring the final cross-sectional area reduction of fractured flat specimens is challenging, as the fracture surface often is not perpendicular to the tensile direction and the cross-sectional geometry in the neck may change during deformation. DIC is therefore useful for studying the failure strain of flat specimens. However, the strain of an element at the localized neck may vary significantly depending on its relative position to the neck. Hence, the maximum element strain found on the specimen is dependent on the position of the mesh. Khadyko et al. [22] reduced the mesh dependence of their results by running several DIC analyses for each tensile test and translating the mesh a certain number of pixels between each analysis. The element strains above a given threshold in all the analyses were then averaged, providing a comparable measure of the ductility throughout the tests. While being a systematic and robust approach, it requires running a large number of DIC analyses. A more manual approach was chosen in the current study, requiring less analyses, and with a repeatability of the results suggesting that it is a consistent measure. The approach is described in the following and illustrated in Fig. 5.

For each test a preliminary DIC analysis with a mesh covering the whole gauge area of the tensile test was studied. The DIC analyses used to achieve the stress–strain curves and data presented above were used as the preliminary analyses. The element size applied was approximately 25×25 pixels. The last frame before failure in the test was then considered. First, the interpolated strain field provided by eCorr was studied, assessing the localization of the strain. The field of DIC residuals was also studied to identify any cracks on the surface affecting the strain field. For tests without any cracks and with the strain distributed across the width of the specimen in a uniform localized neck, as shown in Fig. 5a, the middle row of the mesh was chosen for further adaption. On this row, the element strains of a group of three elements crossing the neck were studied, as illustrated in Fig. 5b. For efficiency, parts of the mesh in the gauge area far away from the neck were removed. The mesh was then translated laterally and the analyses were rerun until the element strain of the outer two elements was approximately balanced, as shown in Fig. 5c. The failure strain measure was then taken as the effective strain of the middle element, defined by the von Mises strain $\varepsilon_{\mathrm{eff}} = \sqrt{\frac{4}{3}\left(\varepsilon_1^2 + \varepsilon_1\varepsilon_2 + \varepsilon_2^2\right)}$, where ε_1 and ε_2 are the principal logarithmic strains. Some tests showed cracks in the field of DIC residuals before specimen failure, and in these cases, the failure strain was either searched for at the element row beyond the crack tip, or where the crack

tests suggests that the inner wall material has a slightly lower yield strength and a lower UTS than the outer wall material. This is not surprising, considering that the inner wall has undergone a lower cooling rate than the outer wall after exiting the extrusion press. A lower cooling rate was shown by Hoang et al. [19] to reduce the yield and tensile strength of an AA6060 alloy due to the formation of non-hardening

(a)

(b)   (c)

Fig. 5. Illustration of the procedure used to establish the ductility measure. (a) The interpolated strain field of a specimen with a uniform localized neck across the width and with no cracks. (b) The longitudinal element strain of three adjacent elements on the middle row crossing the neck is chosen for further study. (c) The mesh is translated laterally and the analysis is rerun until the two outer elements' strain is approximately balanced. The ductility measure is taken as the effective strain in the middle element.

appears, but at the previous frame. For tests where the strain clearly localized towards a part of the specimen, that is, when the strain was not evenly distributed over the width, a row in this part was chosen as the search area.

The results using the above approach are presented in Table 3, and the reasonably small scatter of the values indicates that the approach yields consistent results. It is noted that this should not be interpreted as an absolute measure of the failure strain, as the mesh size was not small enough to capture the maximum local strain. However, the size was constant throughout the analyses, and the measure is hence considered valid for comparison. The results show that there is a significant increase in ductility with increased pre-stretch of the AA6063-profiles. For AA6082, the increase is smaller, and not as certain due to the relatively large scatter compared to the observed increase. The scatter is also too large to conclude on possible differences in ductility between the inner and the outer wall materials, except for AA6063 pre-stretched 0.5%, where the inner wall has clearly higher ductility than the outer wall. In most configurations AA6063 is markedly more ductile than AA6082, except for the outer wall of the 0.5% pre-stretched profiles, where the difference in ductility is small.

3.4. Fractured specimens

Ductile, flat tensile specimens first form a diffuse neck, followed by a localized neck within the diffuse neck area. The width of the localized neck is similar to the thickness of the specimen, and forms at an angle to the tensile direction [23]. By studying the fractured tensile test

Table 3
Measured failure strain based on 2D-DIC with element size 1.1 mm × 1.1 mm.

Alloy	Pre-stretch	Inner/outer wall (i/o)	Failure strain
AA6063	0.5%	i	0.52
			0.53
			0.54
		o	0.40
			0.41
			0.40
	4%	i	0.71
			0.67
			0.69
		o	0.68
			0.74
			0.72
AA6082	0.5%	i	0.26
			0.32
			0.34
		o	0.35
			0.34
			0.31
	4%	i	0.35
			0.40
			0.37
		o	0.35
			0.40
			0.42

specimens, it was found that some of the tests had clearly formed a localized neck, visible as a local reduction of the thickness at the fracture. In some tests the fracture was inclined across the width of the specimen. This is considered an indication of ductility, since the localized neck should be significantly evolved for the fracture to be inclined. The extremes were: AA6063 pre-stretched 4%, where the fracture of all specimens was inclined across the width and there was a pronounced localized reduction of the thickness; and AA6082 pre-stretched 0.5%, where the fracture across the width was straight and across the thickness slant fracture was clearly seen. This is shown in Fig. 6. The 0.5% pre-stretched AA6063-specimens mainly exhibited inclined fracture across the width and slant fracture across the thickness, while the 4% pre-stretched AA6082-specimens mostly experienced fractures somewhere between straight and inclined across the width, and slant fracture across the thickness. There was generally little difference between the fracture characteristics of the inner wall and the outer wall specimens. The exception to this was AA6063 pre-stretched 0.5%, shown in Fig. 7. However, still only small differences were seen. In this case, the outer wall specimens exhibited slant fracture, while the fracture mode of most inner wall specimens was closer to cup–cup. It is noted that this was also the only material configuration with a distinct difference in ductility between the inner and outer wall, as discussed in Section 3.3.

It was further observed that the gauge area of the AA6082-specimens had a distinctive orange-peel surface, while this was not the case for the AA6063-specimens. This agrees well with the grain structures seen in Fig. 3, as orange peeling appearing during deformation is associated with large grains at or just below the surface [21].

3.5. Strain fields from DIC

Fig. 8 shows the interpolated strain fields from one representative test of each outer wall material at the last frame before specimen failure. The specimens of AA6063–4% and AA6082–4% both show a uniform localized neck. The angle of the localized neck is around 20° to the transverse direction of the specimen. The AA6063–0.5%-specimen also shows a localized neck, but the strain is more localized towards the lower part. The AA6082–0.5%-specimen, on the other hand, has a clear localization in the middle part of the specimen. However, one can see a
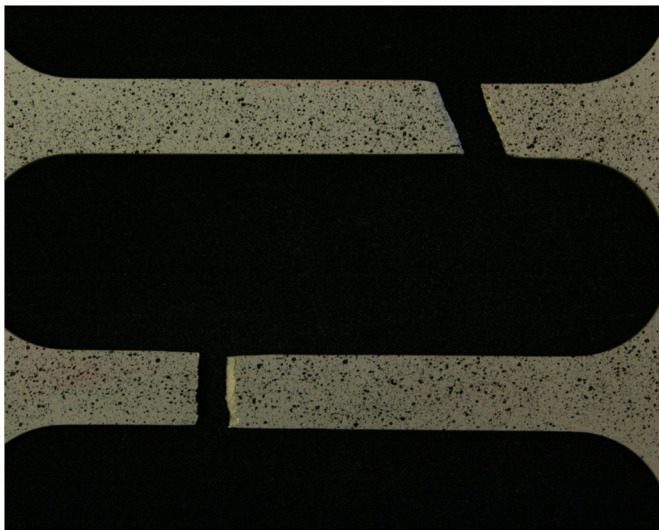
(a) AA6063–4% above, AA6082–0.5% below.
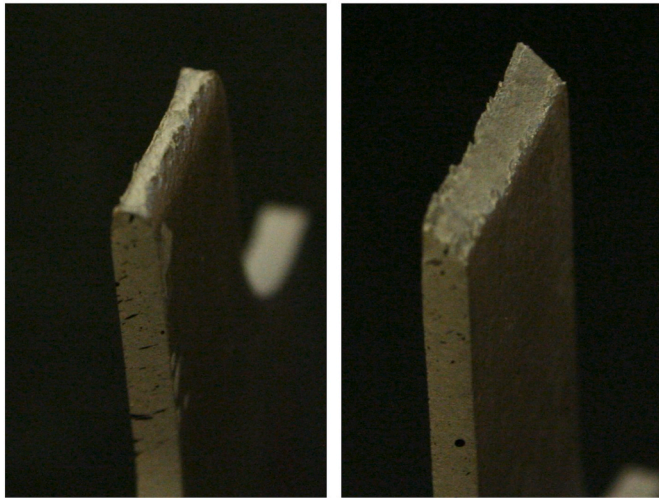

(b) AA6063–4%.   (c) AA6082–0.5%.

Fig. 6. Pictures of fractured tensile test specimens of AA6063–4% and AA6082–0.5%, i.e., the materials with the most and the least ductile fracture modes that were seen, respectively. (a) shows the fracture across the width. (b) and (c) show the fractured end of one AA6063–4%-specimen and one AA6082–0.5%-specimen, respectively.

cross-shape of higher strains, so there are signs of the strain beginning to localize into the inclined bands. One can also see the cross-shapes, but with lower magnitudes of strain, other places in the gauge area.

3.6. TEM studies of the undeformed and deformed outer wall materials

TEM specimens were prepared from the undeformed parts (heads) of the tensile test specimens of the four outer wall materials: AA6063 with 0.5% pre-stretch, AA6063 with 4% pre-stretch, AA6082 with 0.5% pre-stretch and AA6082 with 4% pre-stretch. Due to the thin walls of the profile, the TEM observation direction was perpendicular to the plane of the tensile test specimen and the extrusion direction. The cut slices were thinned down to around 100 μm of the mid-thickness material, punched into 3-mm diameter discs, and electropolished with a TenuPol-5 machine using a mixture of 1/3 HNO_3 and 2/3 methanol kept at − 25 °C and a voltage of 20 V. The characterization was performed with a Jeol JEM-2100 TEM equipped with a LaB_6 filament, operated at 200 kV and used in bright field (BF) and dark field (DF) modes. As the hardening
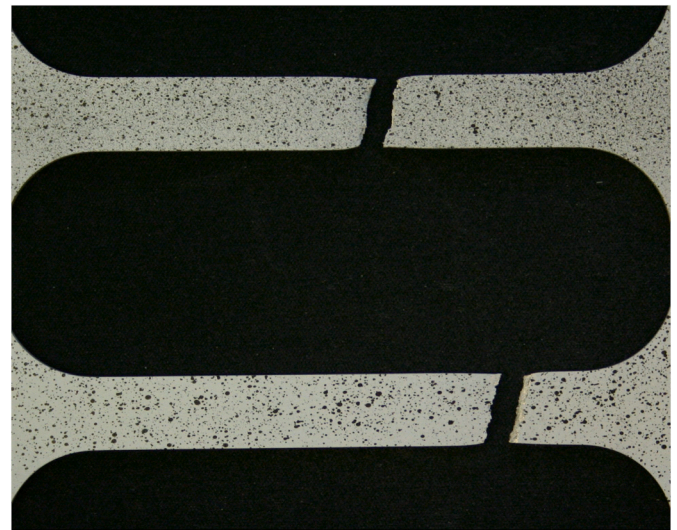
(a) Inner wall specimen above, outer wall specimen below.
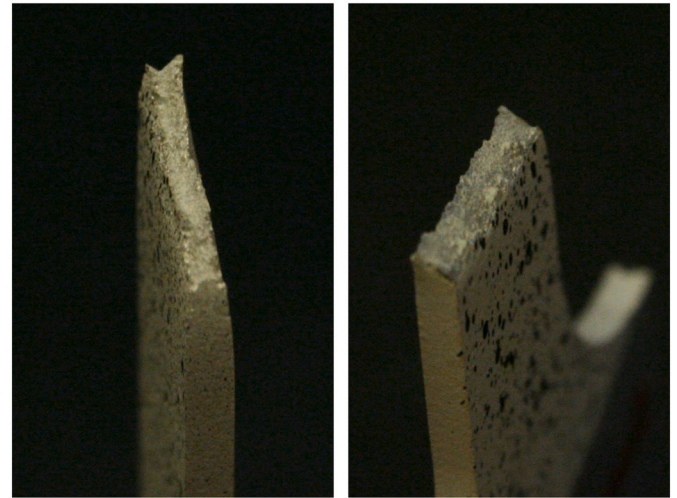
(b) Inner wall specimen.   (c) Outer wall specimen.

Fig. 7. One inner wall and one outer wall specimen of AA6063–0.5%. (a) shows the fracture across the width. (b) and (c) show the fractured end of the inner wall and the outer wall specimens, respectively. The fracture of the inner wall specimen tends slightly towards a cup-cup mode and a distinctly reduced thickness is seen. The fracture of the outer wall specimen tends more towards a slant fracture and the thickness is not as clearly reduced.

metastable precipitates in the 6000-series aluminium alloys are needle-shaped with needle direction along the crystallographic <100>Al directions, they are fully characterized by a set of parameters consisting of the needle number density and the average needle cross section, length and volume fraction. These parameters have been quantified following the methodology described in Ref. [24]. A Gatan imaging filter attached to the TEM instrument was used for specimen thickness measurement. For the 0.5% pre-stretched materials, approximately 200 needle lengths and between 100 and 130 needle cross sections were measured to ensure good statistical accuracy. Between 3000 and 4000 precipitates were counted for the precipitate number density calculations. In the 4% pre-stretched materials, approximately 200 needle lengths in flat areas in-between the dislocation lines and approximately 130 needle lengths of precipitates nucleated on dislocation lines were measured. For cross-sectional areas, approximately 100 precipitates in the flat areas and 100 precipitates nucleated on dislocation lines were measured. Between 2000 and 4000 precipitates nucleated in flat areas and
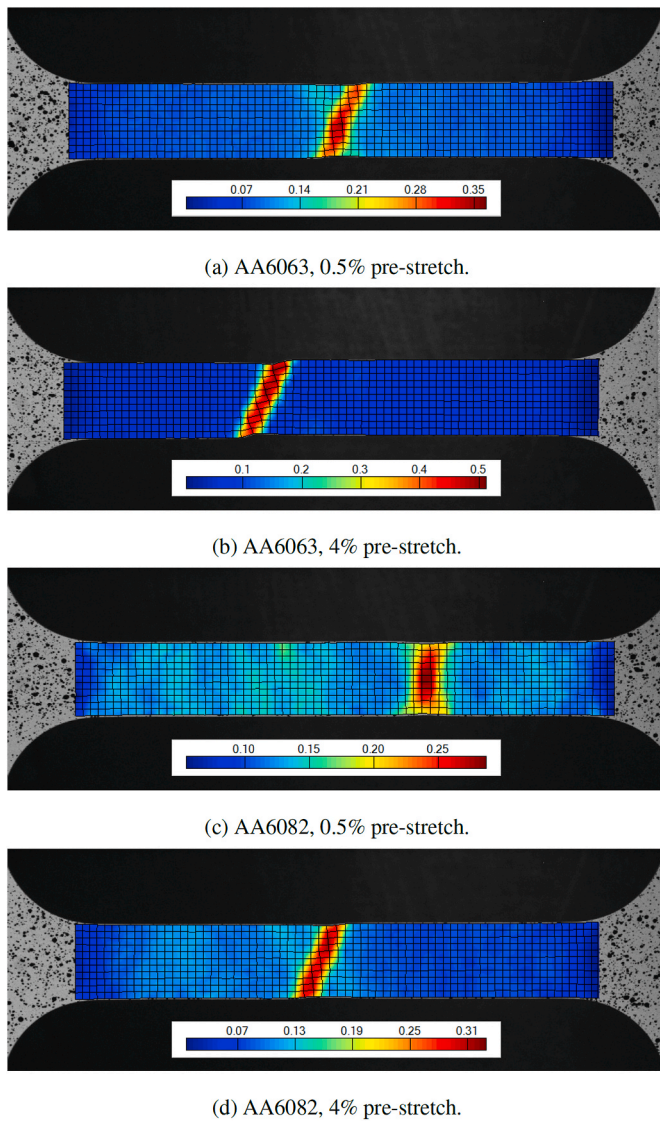
(a) AA6063, 0.5% pre-stretch.

(b) AA6063, 4% pre-stretch.

(c) AA6082, 0.5% pre-stretch.

(d) AA6082, 4% pre-stretch.

Fig. 8. Interpolated strain fields in the last frame before fracture from one representative test of each outer wall material.

approximately 1500 precipitates nucleated on dislocation lines were counted.

Fig. 9 shows typical examples of microstructures for both pre-stretches of the AA6063 and AA6082 alloys. While in the BF images all the microstructure constituents are visualised (needle precipitates viewed along and perpendicular to their lengths, as well as dislocation lines), only the distribution of precipitates viewed along their needle lengths is highlighted in the DF images. From these and similar images some important observations can be made. AA6063 has a lower precipitate density than AA6082. This is due to the lower total solute level of the former. The 4% pre-stretch is introducing dislocation lines which become preferred nucleation sites for coarse precipitates. Still, the dislocation density is low enough to allow the existence of flat areas in-between them. Some of these areas become islands with denser precipitation of smaller needles, resembling bulk precipitation. Therefore, the microstructure in the higher pre-stretched alloys becomes more inhomogeneous, consisting of larger precipitates nucleated on dislocation lines and dense precipitation in some flat areas in-between the dislocations. When the dislocation density is higher locally, precipitate-free zones are observed in their vicinity (with no dense precipitation). Because AA6063 has an overall lower precipitate density and most of its precipitates are nucleated on dislocation lines, the precipitate density in

the flat areas is lower than in AA6082. For both alloys, the overall result of increased pre-stretch is a coarsening of the microstructure (lower density of larger precipitates), which may be defined as an accelerated overageing. These results are in line with previous studies [15].

In the 4% pre-stretched materials, the split of precipitation in coarse needles nucleated on dislocation lines and dense, smaller needles in the flat areas allowed the separation of precipitate statistics for these two cases. The results are listed in Table 4. For the 0.5% pre-stretched materials only one case is considered, as nearly all the precipitates are of the dense type nucleated homogeneously in the bulk.

The values in Table 4 support the above observations. It is interesting to notice that the overall precipitate density drop due to the increased pre-stretching is similar for both alloys, while the relative number of precipitates nucleated on dislocations in the total microstructure is higher in AA6063. A consequence of this is a stronger coarsening effect due to pre-stretching in AA6063, as it contains the largest precipitates in the 4% pre-stretched condition.

Following the characterisation of hardening precipitates as function of alloy composition and pre-stretching, the four conditions in Table 4 were subjected to further stretching until fracture. The resulting microstructures were investigated in areas close to the neck of the tensile test samples. TEM specimen preparation for these conditions was performed with the same procedure as for the undeformed material taken from the heads of the tensile test samples described above. The deformed conditions are useful in studying how the newly introduced dislocations interacted with the needle precipitates and the dislocations from pre-stretching. Representative micrographs are shown in Fig. 10. The most important result of this interaction is the formation of dislocation cells, with the strongest effect in the 4% pre-stretched AA6063 alloy, and the weakest in the 0.5% pre-stretched AA6082 alloy. AA6082 pre-stretched 4% and AA6063 pre-stretched 0.5% looked similar. When these observations are connected to the microstructure investigations described above and quantified in Table 4, it can be concluded that the tendency to form dislocation cells is enhanced by a reduced precipitate number density and by the coexistence of soft, flat areas (with low bulk-like precipitate density) with hard areas having dislocation lines with precipitates nucleated on them. How these observed differences in the microstructure affect the material behaviour will be discussed in Section 6.

4. Component tests

4.1. Specimens and experimental set-up

The components of each material configuration were all taken from the same extruded profile, which after extrusion was stretched to 0.5% or 4% plastic strain, then cut into 1 m lengths and artificially aged as specified in Section 2. Subsequently, they were cut by wire erosion into shorter profiles of 350 mm length with a 5° geometrical trigger as illustrated in Fig. 11a, such as used in Refs. [4,9,25]. The cross-sectional geometry was given in Fig. 1. The lower 80 mm of the profiles was constrained by a clamping device during both quasi-static and dynamic testing, hence the effective length of the profiles was 270 mm. The clamping device consisted of an external steel part and internal wooden blocks as shown in Fig. 11b and c. The exact material properties of these parts are not deemed important for the results and the clamping device may be assumed rigid.

The profiles' walls were measured before testing. The wall thickness of the different sections of the profiles varied up to 8.2%. Additionally, the profiles used in the dynamic tests were weighed before testing. The 0.5% and 4% pre-stretched AA6063-profiles were respectively on average 1.2% and 0.3% heavier than the corresponding AA6082-profiles. The reduction in mass of the 4% pre-stretched profiles compared to the 0.5% pre-stretched profiles was 4.7% for AA6063 and 3.8% for AA6082. The scatter in mass between equivalent profiles was considered negligible, as the difference between the lightest and
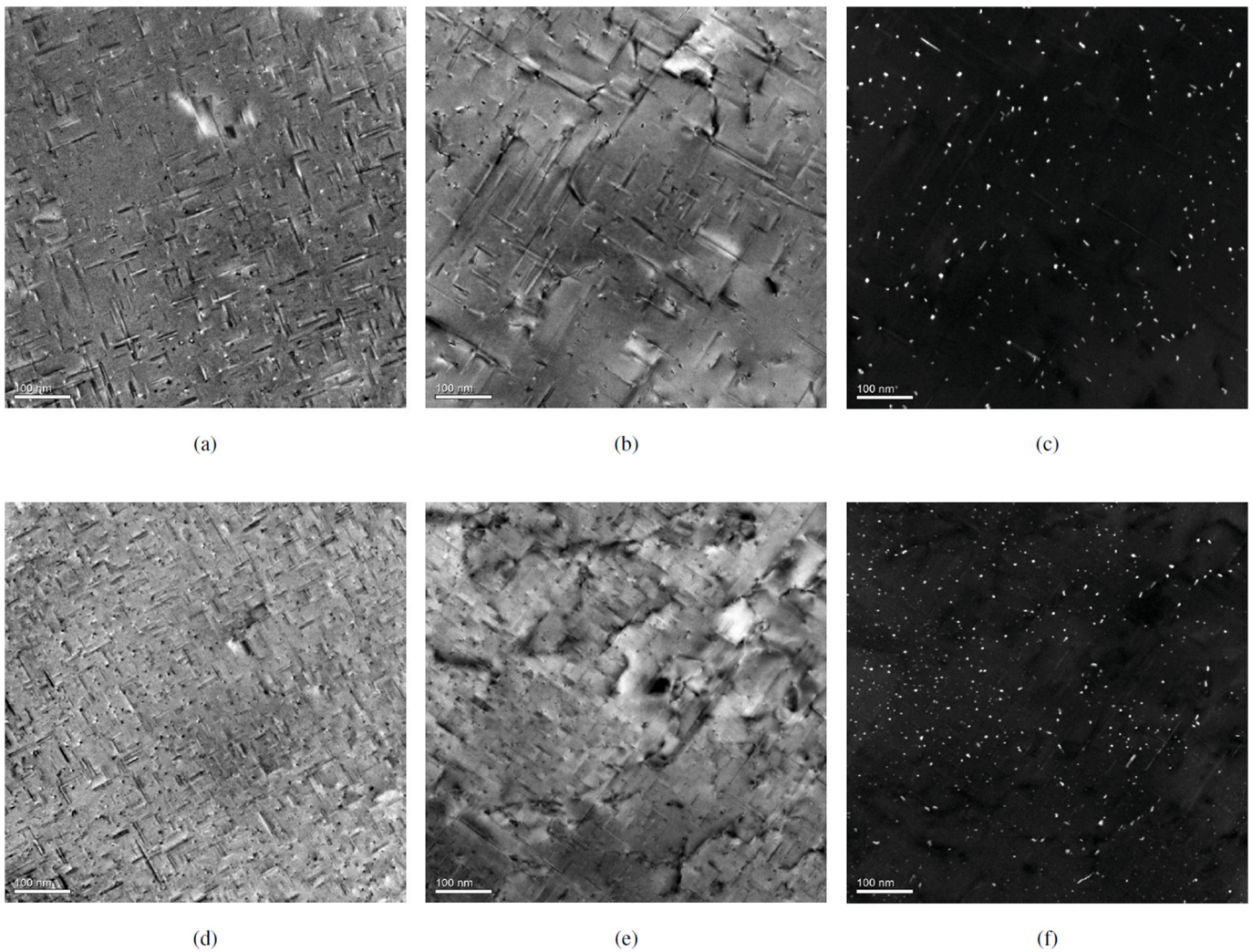
Fig. 9. (a), (b) BF images of AA6063 pre-stretched 0.5% and 4%, respectively; (d), (e) BF images of AA6082 pre-stretched 0.5% and 4%, respectively. (c) and (f) are the corresponding DF images of (b) and (e), respectively. All images are recorded with the matrix oriented along a <001>Al direction. The slice thickness in all images is between 65 and 75 nm.

heaviest profile within a profile series was between 0.01% and 0.4%.

4.1.1. Quasi-static crushing test set-up

The quasi-static crushing tests were performed in an Instron 5985 universal testing machine with a 250 kN load cell at 10 mm/min. The deformation was captured by two synchronized Prosilica GC2450 cameras at 1 Hz with a resolution of 2448 × 1228 and 2448× 1137 pixels, while the force and displacement were logged by the machine at 10 Hz. Three repetitions of each test were performed. The tests were run to 140 mm displacement before being stopped.

4.1.2. Dynamic crushing test set-up

The dynamic crushing tests were performed in SIMLab's kicking machine, thoroughly described in Ref. [26], with a 400 kg trolley at impact velocities of 8, 10 and 12 m/s. In the kicking machine, a pendulum is accelerated by a hydraulic–pneumatic system. The pendulum further accelerates a trolley towards the test specimen that is mounted to a 150-tonne reaction wall. The machine has been used with success in several impact studies. Examples on studies with aluminium components are crushing of profiles [9], impact of bumper systems [26] and low-velocity impact of stiffened panels [27]. To have comparable results to the quasi-static tests, the trolley should not be completely stopped before 140 mm displacement, while avoiding any excessive additional displacement. A minimum velocity of 7–8 m/s was estimated

for reaching at least 140 mm displacement. For the displacement of the impactor not to overly exceed the desired 140 mm, two buffers were placed on the sides of the specimen to provide additional resistance for decelerating the trolley. The buffers each consisted of four square aluminium profiles cut to an appropriate length such that they were impacted by the trolley after the desired displacement was reached. It should be noted that in the following section, the energy absorption of the dynamic tests is taken at the point in time when the impactor's displacement is 140 mm, for comparability with the results from the quasi-static tests. The deformation was captured by a Phantom v2511 high-speed camera with 1280 × 720 pixels resolution at 25 kHz. The load cell had a sampling frequency of 250 kHz. The force data was filtered by a low-pass zero-phase 2nd order Butterworth filter with a cut-off frequency of 12 kHz, filtering out high-frequency noise from the force–displacement curves.

4.2. Experimental results

4.2.1. Quasi-static tests

The results of the quasi-static crushing tests are given in Table 5 and Fig. 12. The mean force is included in Table 5, but will not be discussed when comparing the materials due to different profile masses among the test series. The repeated tests were very consistent, both in peak force and energy absorption. The scatter in energy absorption was smallest for

Table 4
Parameters of needle precipitates in the investigated conditions.

Needle parameter		AA6063 0.5% pre-stretch	AA6063 4% pre-stretch	AA6082 0.5% pre-stretch	AA6082 4% pre-stretch
Number density (μm^{-3})	Bulk	33020 ± 4186	11109 ± 1255	73149 ± 7670	35378 ± 3684
	On disloc.	–	3853 ± 1276	–	5592 ± 982
	Overall	33020 ± 4186	13921 ± 2282	73149 ± 7670	34428 ± 4081
Length (nm)	Bulk	38.18 ± 2.64	34.37 ± 1.75	30.02 ± 0.98	18.91 ± 0.74
	On disloc.	–	166.48 ± 30.39	–	104.06 ± 9.63
	Overall	38.18 ± 2.64	78.88 ± 8.20	30.02 ± 0.98	46.89 ± 2.16
Cross section (nm^2)	Bulk	8.18 ± 0.46	8.47 ± 0.44	5.87 ± 0.29	4.74 ± 0.37
	On disloc.	–	14.50 ± 0.75	–	17.69 ± 1.19
	Overall	8.18 ± 0.46	11.55 ± 0.48	5.87 ± 0.29	10.27 ± 0.73
Volume fraction (%)	Bulk	1.03 ± 0.21	0.32 ± 0.05	1.29 ± 0.17	0.32 ± 0.04
	On disloc.	–	0.93 ± 0.52	–	1.03 ± 0.29
	Overall	1.03 ± 0.21	1.27 ± 0.36	1.29 ± 0.17	1.66 ± 0.28

the test series with the least fracture, and largest for the test series exhibiting most fracture. As seen in Fig. 12a and b, some of the force–displacement curves within each series were also practically identical, as was the deformation and the visible fracture in some of the profiles. Hence, the overall repeatability of the quasi-static tests is considered excellent.

It was clear from studying the exterior of the profiles, that there was more fracture in the 0.5% pre-stretched profiles than in the 4% pre-stretched profiles of both alloys and more fracture in the AA6082-profiles than in the AA6063-profiles. Thus, the quasi-static crushing tests showed the same trends in ductility as the tensile tests. No fracture was found in the AA6063–4%-profiles by visual inspection, while all the other materials were clearly fractured. The transition between the inner and the outer wall, i.e., the T-junction, seemed to be a typical location for fracture to occur. This is shown for: AA6063–0.5% in Fig. 13a, where the inner wall tore and the outer wall at the lowermost lobe subsequently fractured and folded out; and for AA6082–4% in Fig. 13d, where the outer wall tore along the transition to the inner wall. These fracture modes seemed to be provoked by a change in deformation mode. As long as the profile folded according to Fig. 14a, here denoted mode A, there appeared to be little fracture for the more ductile materials. However, the folding tended to change towards the mode illustrated in Fig. 14b, here denoted mode B, which seemed to cause particularly high strains on the T-junction, causing fracture in this region. Except for cracking in the corners of AA6082–4%, AA6063–0.5% and AA6082–4% seemed to have little fracture beyond what was caused by the change in deformation mode. AA6082–0.5%, on the other hand, had large amounts of fracture without the deformation mode change, see Fig. 13c. These profiles mostly kept to the mode A folding, presumably caused by fracture. The mode B folding also appeared to cause the force–displacement curve, as best seen in Fig. 12a, to form larger and more distinct fluctuations, while it had a much flatter and more even appearance in the beginning, after the initial peak, when the profile deformed according to mode A.

The specific energy absorption of AA6063 was lower for the 4% pre-stretched profiles than for the 0.5% pre-stretched profiles, while for AA6082, there was little difference between 0.5% and 4% pre-stretch. Hence, it may seem that for AA6063, the increase in ductility caused by higher pre-stretching is not sufficient to compensate for the effect of the lower strength. For AA6082, the yield strength was higher but the UTS lower for the higher pre-stretched profiles compared to the lower pre-stretched profiles. It is thus difficult to claim whether the ductility was determinant for the energy absorption. This will be further discussed in Section 6.

4.2.2. Impact tests

The results from the dynamic tests are seen in Table 6 and in Figs. 15 and 16. As in the quasi-static tests, the specific energy absorption was higher for AA6082 than for AA6063, and for AA6063, the specific energy absorption was higher for the 0.5% pre-stretched profiles than for the 4% pre-stretched profiles. The results indicate a higher energy absorption for the 4% pre-stretched AA6082-profiles than for the 0.5% pre-stretched profiles in the dynamic case. However, there is a certain scatter in the energy absorption for the AA6082-profiles, and the energy absorption for the 4% pre-stretched profiles is not strictly higher than the energy absorption for the 0.5% pre-stretched profiles.

The deformation pattern of one profile of each material configuration is shown in Fig. 17. More fracture was observed in the 0.5% pre-stretched profiles than in the 4% pre-stretched profiles of both alloys and in the AA6082-profiles than in the correspondingly pre-stretched AA6063-profiles, as was also observed in the quasi-static tests. Much more variation was seen in the deformation pattern of the profiles in the dynamic tests than what was seen in the quasi-static tests. This extends to the force–displacement curves, which are not coincident within each test series. One trend in the deformation pattern with velocity was seen. When increasing the impact velocity from 10 to 12 m/s, the first fold was altered in a similar manner for all the material configurations. After the initial peak in the mean force curves of AA6063–0.5%, AA6063–4% and AA6082–4% in Fig. 16 the curve for the 12 m/s-test is higher than the curves for the tests at the other impact velocities, which could indicate an effect from this mode change on the force level. Compared to the quasi-static tests, there was more variation in the total energy absorption in the dynamic tests, but there was no unique trend in the energy absorption with impact velocity. It was observed that the folding pattern throughout the series may differ quite much, but the energy absorption has comparably little variation.

Despite low strain-rate sensitivity, low strain hardening and moderate impact velocities, the peak force and the energy absorption were higher in the dynamic tests than in the quasi-static tests, presumably due to inertia effects. The peak force had an average increase within each test series of between 20 and 50% from the quasi-static case. The energy absorption was increased for all material configurations compared to the quasi-static tests, by 15% on average. It is observed that the lowest average increase in energy absorption is found for the material with most fracture, i.e., the 0.5% pre-stretched AA6082-profiles. For AA6082, in particular the 0.5% pre-stretched profiles, the buckling pattern involved a smaller length of the profiles than for the profiles of the other materials at the same impacting displacement, as can be seen in Fig. 17. This was caused by the large amount of fracture facilitating compression of the folds at the expense of new folds developing. It was difficult to
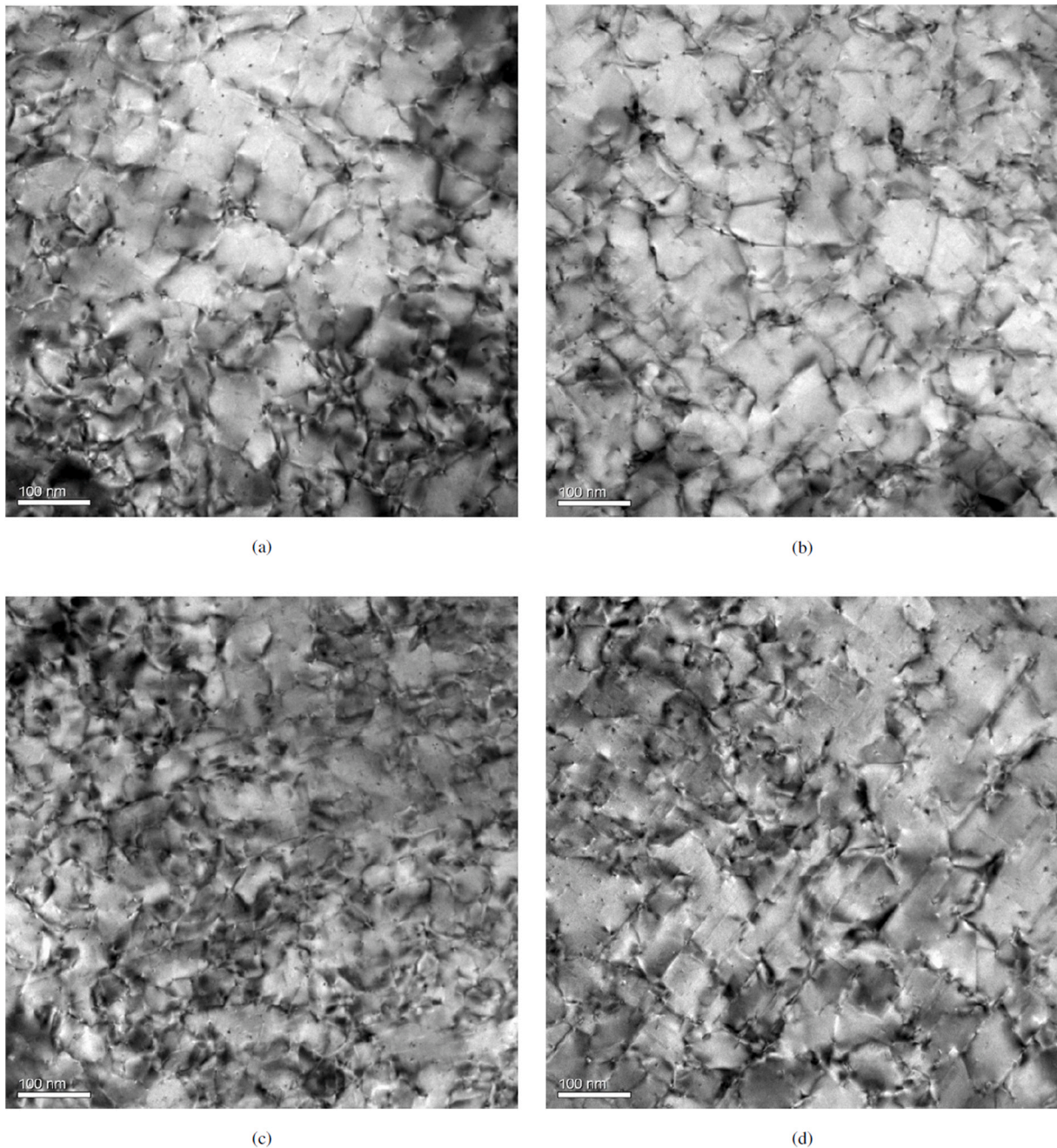
Fig. 10. BF images taken close to the neck of tensile test samples, having the matrix oriented along a <001>Al direction. (a) AA6063 pre-stretched 0.5%, (b) AA6063 pre-stretched 4%, (c) AA6082 pre-stretched 0.5%, (d) AA6082 pre-stretched 4%.

compare the amount of fracture of the impacted AA6063-profiles to the quasi-statically tested profiles by visual inspection and conclusions in this regard requires more thorough investigation. The tendency of the deformation mode changing from mode A to mode B, with the associated fracture modes seen in the quasi-static tests, was reduced. However, other fracture modes occurred in the dynamic tests and the T-junction was still fractured in the profiles where the deformation mode did not change to mode B. Very small amounts of fracture were found at the T-junction in the impacted AA6063–4%-profiles, but so little that it was not reasonable to conclude on a less ductile behaviour than for the quasi-statically tested profiles. The AA6082-profiles, on the other hand, were clearly more extensively fractured in the impact tests than in the quasi-static tests. The folds were fractured along the corners and the T-junction, and horizontally, causing the fractured walls to peel out from the

profile, which was most prominent in the 0.5% pre-stretched profiles. This behaviour was also seen to a much lower extent in the quasi-static tests of the 0.5% pre-stretched profiles, while it did not occur in the quasi-static tests of the 4% pre-stretched profiles.

5. CT scans of the deformed profiles

5.1. Method

To study fracture of the profiles more extensively, one quasi-statically and one dynamically tested profile of each material configuration were CT-scanned. The scans were performed in the X-ray CT laboratory at the Department of Physics at NTNU using a Nikon XT H225 ST MicroCT machine.
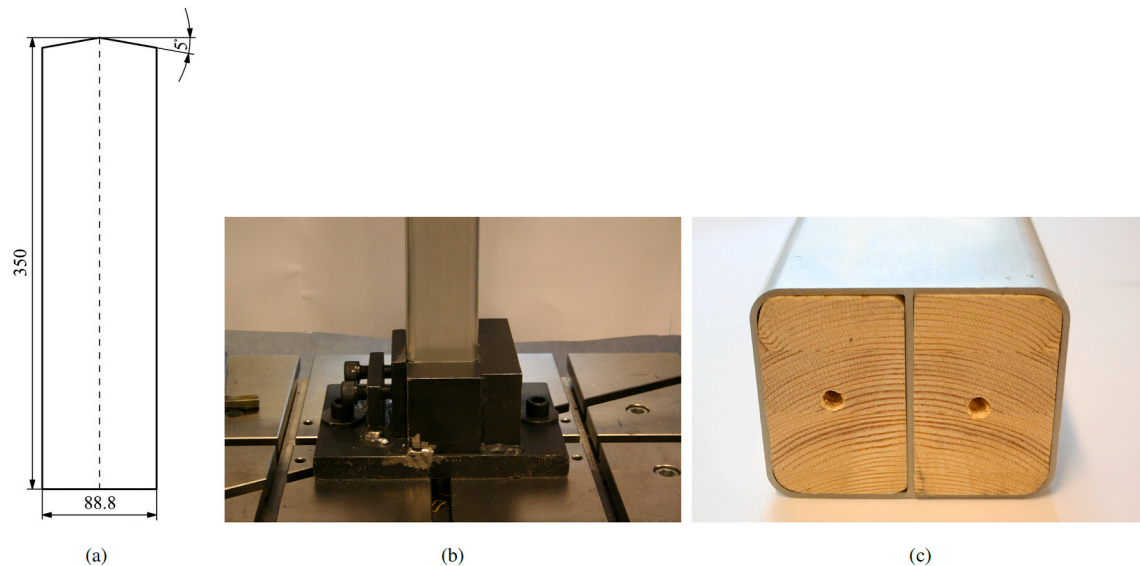
Fig. 11. (a) Geometry of the cut profiles. (b) The clamping device used for both the quasi-static and the dynamic tests, here shown in the quasi-static test set-up. (c) The wooden blocks used as the internal part of the clamping device.

Table 5
Results of the quasi-static crushing tests. The specific energy absorption is found as the mean force multiplied by the total displacement and divided by the mass of the entire profile.

Alloy	Pre-stretch	Peak force (kN)	Mean force (kN)	Specific energy absorption (kJ/kg)
AA6063	0.5%	123.06	65.05	13.12
		124.14	64.97	13.11
		124.37	65.51	13.23
	4%	112.79	59.23	12.53
		112.80	58.74	12.42
		111.93	58.76	12.44
AA6082	0.5%	140.18	70.90	14.48
		139.81	70.19	14.34
		140.46	68.51	13.99
	4%	136.00	68.53	14.53
		136.42	68.48	14.53
		136.46	67.34	14.30

It is emphasized that the scans are done after testing, i.e., of the profiles' final deformed state, whereas data and pictures presented in the previous section were all taken at 140 mm crushing distance. As the quasi-static tests were stopped immediately after reaching 140 mm, the CT scans of the quasi-statically tested profiles are consistent with the data presented in the previous section. However, in the dynamic tests, the final trolley displacement was more than 140 mm, and the CT scans hence present the profiles at a later stage of deformation than what was presented in the previous section. It follows that the amount of fracture may have increased, and this should be taken into account when considering the scans. The ultimate trolley displacement of the dynamic test specimens that were CT-scanned was 158–159 mm.

The reconstructions of the scans were made using the programme Nikon CT Pro 3D, Version XT 4.4.2. The reported voxel size was 74 μm. The scans were then studied in ImageJ 1.52a [28] and ParaView 5.7.0-RC1 [29]. ImageJ was used to scroll through series of 2D-slices of the profiles in three orthogonal directions, coinciding with the extrusion direction and the transverse directions parallel to the walls. In this way, fracture in the less complex parts of the geometry is easily detected. However, in the more complex zones, that is, the corners and the T-junctions, where lobes in different directions meet, it may be difficult to distinguish between fracture and walls that are almost in contact

using this approach. This is illustrated in Fig. 18, showing one situation where fracture is unmistakable and one where it is not easy to distinguish between fracture and two walls in contact. To study the more complex zones, smaller parts of the image sequences were cut out using ImageJ and rendered as three-dimensional surface models in ParaView. Larger pieces of the profiles, such as the interior of one chamber, were studied by rendering the entire profile in ParaView without cutting in ImageJ first. Simple cuts were then performed directly in ParaView. A common method used for studying crushed profiles is to cut them into smaller pieces to be able to observe both the exterior and the interior of the profiles, such as done in Ref. [25]. In this work, by cutting and rendering CT scans of the tested profiles, a virtual, non-destructive version of this method was applied.

5.2. Observations from the CT scans

Using the above approach, the scans were studied systematically and evaluated qualitatively. Some observations are discussed in the following. Observing characteristics and differences in fracture in the quasi-statically and the dynamically tested profiles was the primary objective. However, recall that the dynamically loaded profiles were more deformed and thus a direct comparison between the scans is not feasible.

Of the 0.5% pre-stretched AA6063 alloy, the quasi-statically and dynamically tested profiles differed in how the T-junction was fractured. In this zone, the quasi-statically tested profile was generally fractured on the inner wall, as shown in Fig. 19a, while the dynamically tested profile was mainly fractured on the outer walls, as seen in Fig. 19b. The remaining parts of the profiles were quite similarly fractured. Both profiles had cracks extending horizontally along the folds from the T-junction and from the corners, and moderate amounts of cracking in the corners. Due to the differences in the fracturing of the profiles, it is difficult to claim whether one is more fractured than the other.

In both 4% pre-stretched AA6063-profiles, no fracture was found in the less complex areas by browsing through the slices in ImageJ, and the T-junctions and corners were difficult to evaluate by this approach. For the quasi-statically tested profile, fracture was neither found when studying larger pieces of the profile in ParaView, except for one of the corners, where there was a small crack below one fold, shown in Fig. 19c. When studying one of the T-junctions, it was also evident that the inner wall was fractured at some places, but the cracks did not seem to have propagated significantly. The impacted profile, on the other
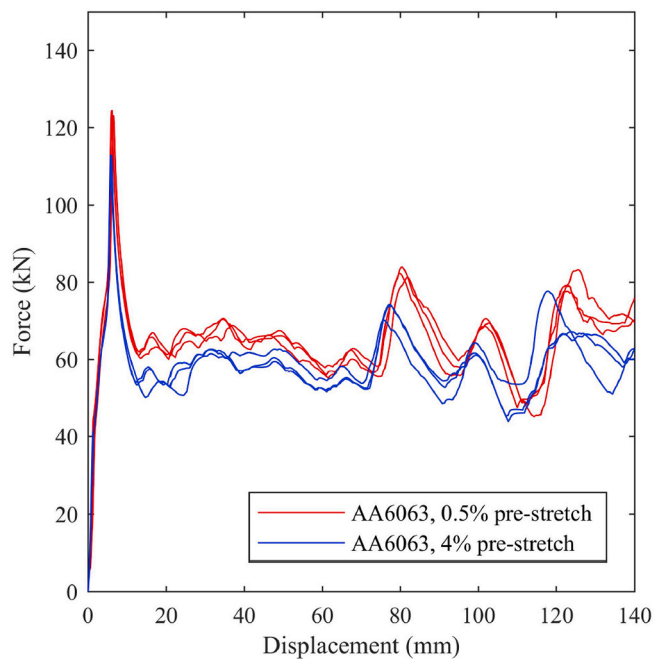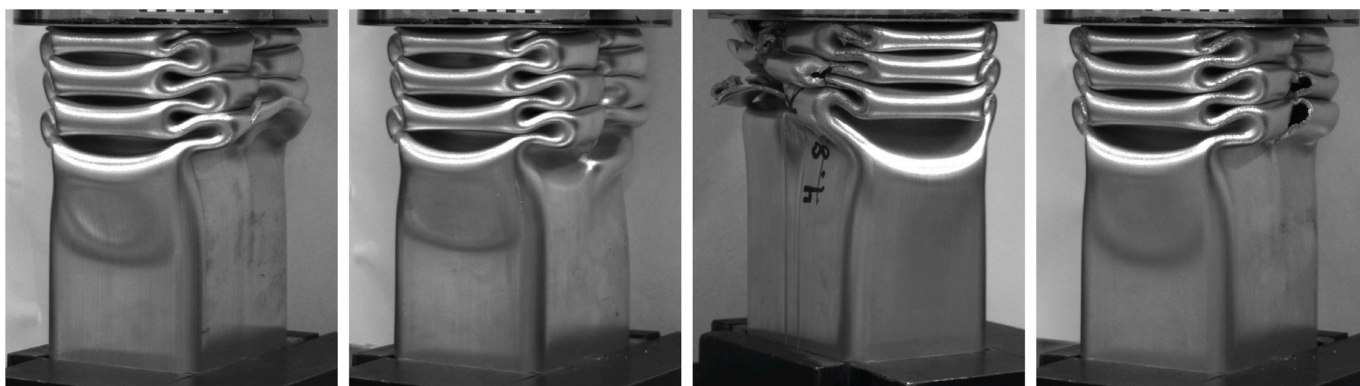
(a) AA6063.
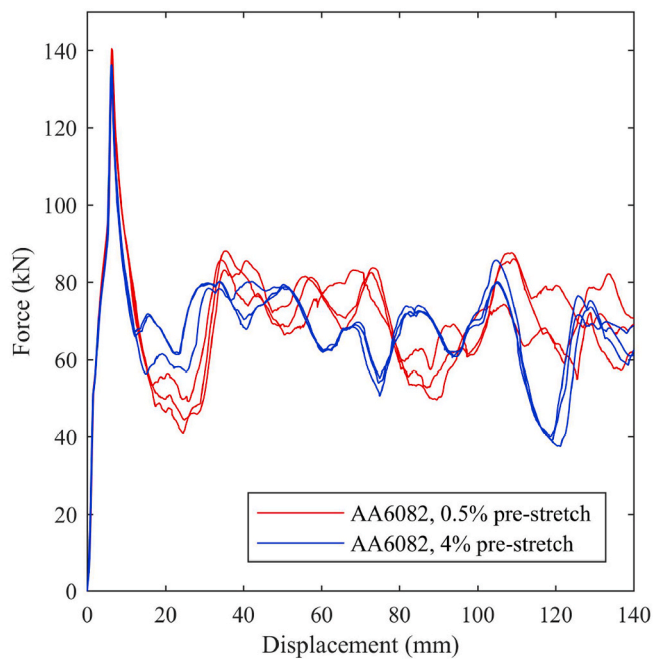
(b) AA6082.

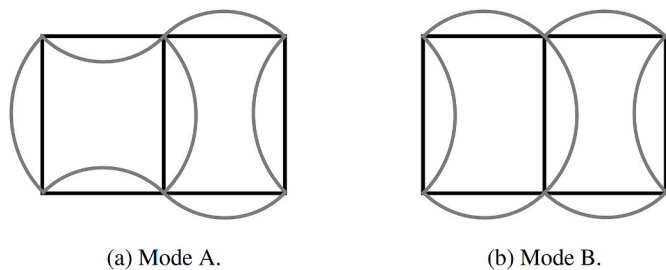**Fig. 12.** Force–displacement curves from the quasi-static crushing tests.

(a) AA6063–0.5%.

(b) AA6063–4%.

(c) AA6082–0.5%.

(d) AA6082–4%.

Fig. 13. The deformation pattern at 140 mm displacement of one representative profile of each material configuration subjected to quasi-static loading.


(a) Mode A.

(b) Mode B.

Fig. 14. Schematic illustration of the two main deformation modes observed in the quasi-static crushing tests. The deformation often started out with mode A (a), then it transitioned to mode B (b).

Table 6
Results from the dynamic crushing tests.

| Alloy	Pre-stretch	Velocity (m/s)	Peak force (kN)	Mean force (kN)	Specific energy absorption (kJ/kg)
AA6063	0.5%	8.08	171.49	74.21	14.97
		9.83	158.67	74.32	14.99
		12.05	178.14	75.22	15.17
	4%	8.01	151.52	69.06	14.59
		10.03	138.04	67.62	14.30
		11.90	161.39	68.50	14.53
AA6082	0.5%	8.08	187.80	78.97	16.12
		10.02	176.85	76.62	15.64
		11.96	171.71	79.35	16.21
	4%	8.00	175.85	75.82	16.09
		9.98	168.02	80.42	17.07
		12.19	176.49	80.85	17.14
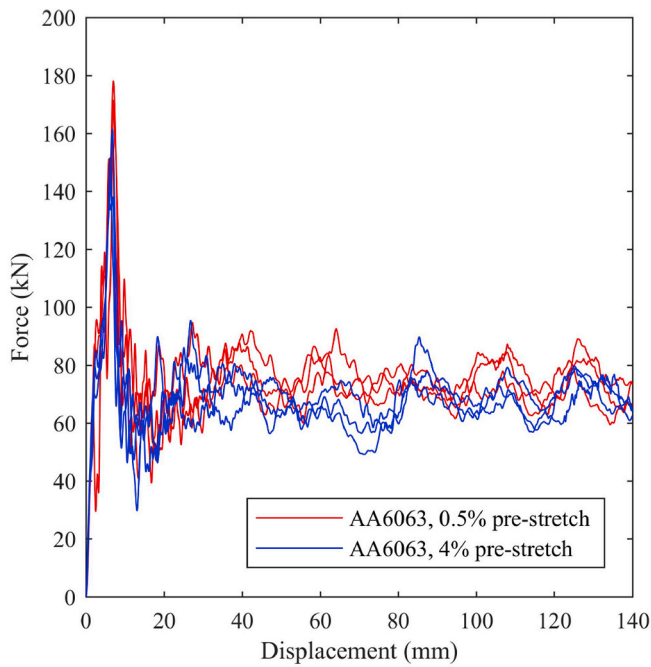
(a) AA6063.
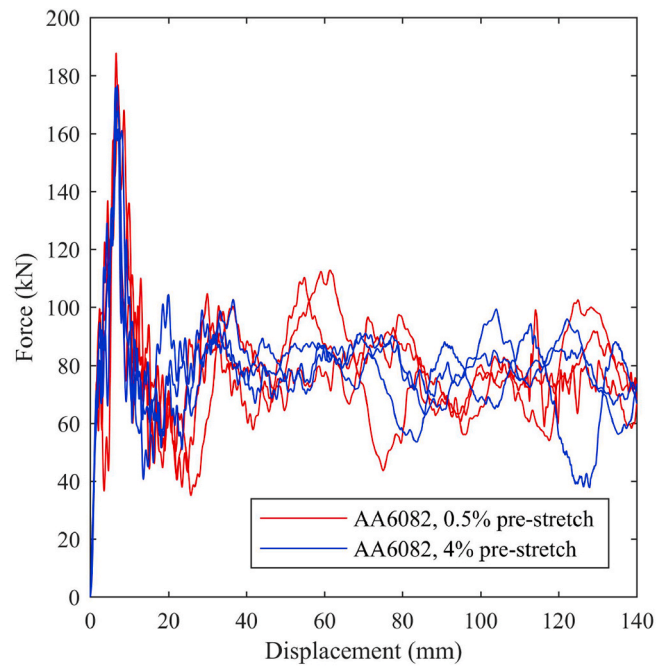
(b) AA6082.

Fig. 15. Force–displacement curves from the dynamic crushing tests. For readability, and due to the lack of evident trends, the curves do not distinguish between the different impact velocities.
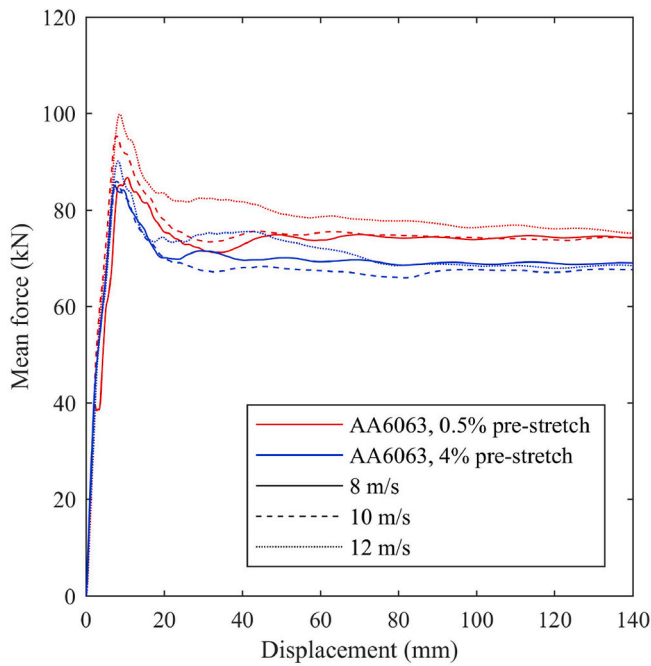
(a) AA6063.
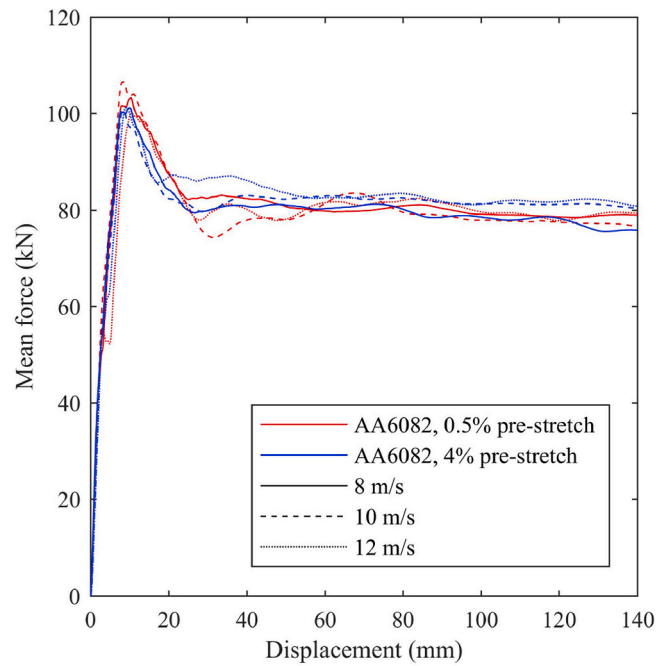
(b) AA6082.

Fig. 16. Mean force–displacement curves from the dynamic crushing tests.

hand, was clearly fractured on the exterior surface of the outer wall at the T-junctions, and when studying the rendered T-junction, it was clear that these cracks extend through the walls, as shown in Fig. 19d. There was also some cracking close to the corners on the lower side of the folds, as was seen in the quasi-statically tested profile.

For AA6082 pre-stretched 0.5%, it was clear from the orthogonal

slices that there was much more fracture in the dynamically tested profile. The lobes in the dynamically tested profile were more compressed than the lobes in the quasi-statically tested profile, as seen in Fig. 20a and b. Although some of this may be attributed to the excessive impact displacement in the tests, comparison with images of the deformed profiles at 140 mm impactor displacement in the previous
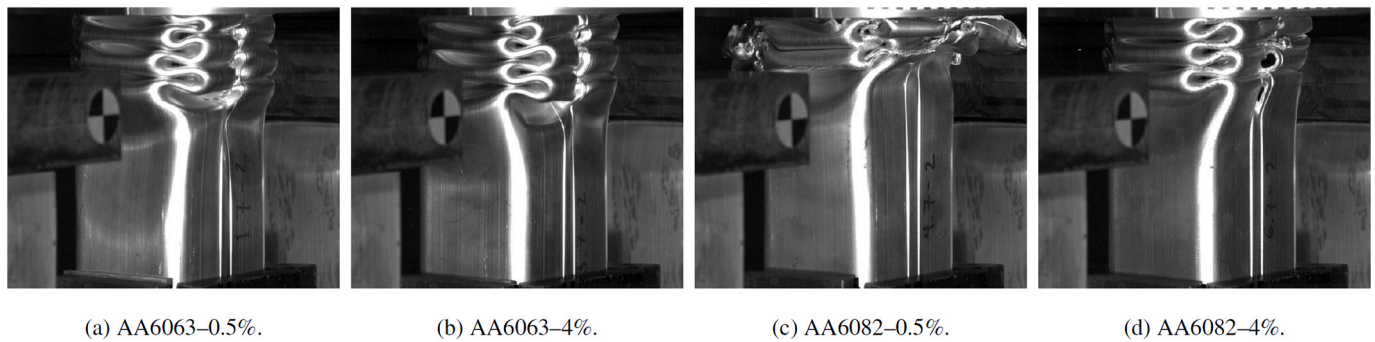
| (a) AA6063–0.5%. | (b) AA6063–4%. | (c) AA6082–0.5%. | (d) AA6082–4%. |

Fig. 17. Deformed profiles after 140 mm trolley displacement. The profiles of each material configuration subjected to 8 m/s impact loading are shown.
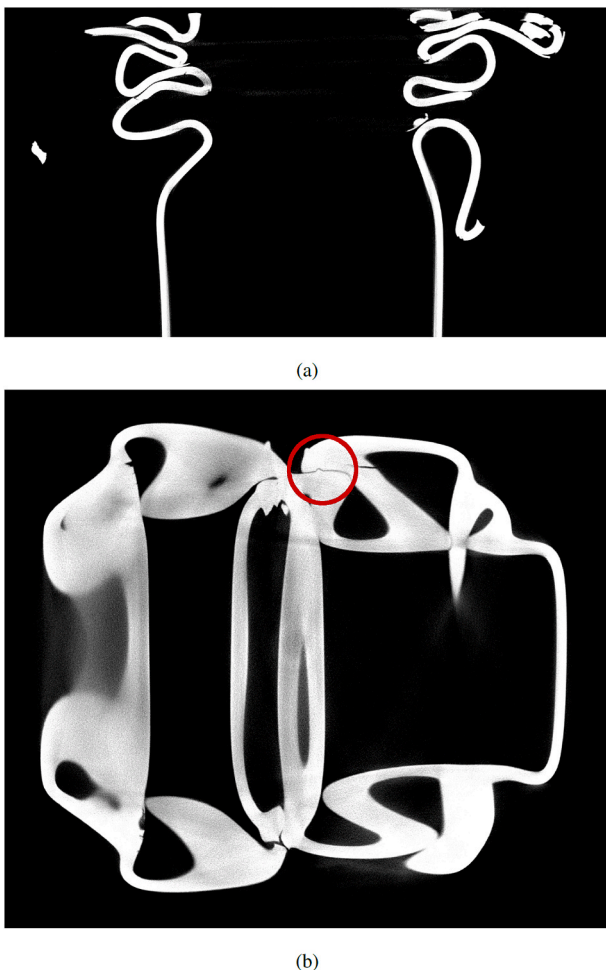

(a)

(b)

Fig. 18. CT scan slices of two deformed profiles which show one case in (a) where fracture is very clear and one case in (b) where fracture is less evident and some geometrical features could easily be misinterpreted as fracture. In (a) the walls are clearly fractured where they are discontinuous in the image. The red circle in (b) accentuates a place where what could be perceived as fracture is just folds in contact. (For interpretation of the references to colour in this figure legend, the reader is referred to the Web version of this article.)

chapter confirmed that the folds of the impacted profile were more compressed. The impacted profile clearly has more fracture through the walls. In several locations of the quasi-statically tested profile, a fracture in which the walls were delaminated was observed. This was not found in the impacted profile.

The quasi-statically and the dynamically tested profiles of the 4% pre-stretched AA6082 alloy were somewhat similarly fractured. Both
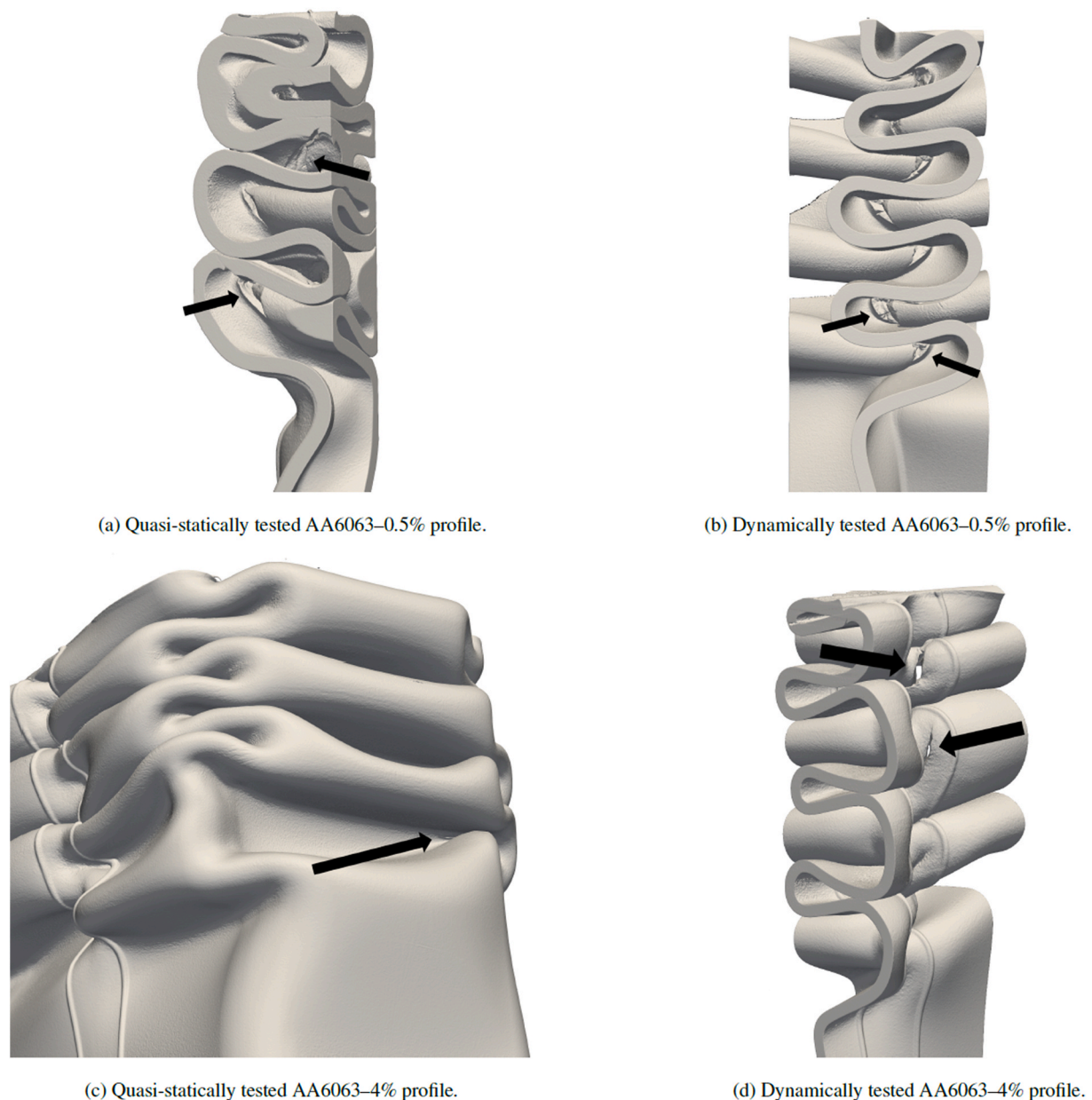
had considerable cracking in the corners and both profiles appear to have torn along the transition from the outer wall to the inner wall. However, in the impacted profile, the fracture of the T-junction also extended horizontally along the folds, as seen in Fig. 20d. As in the 0.5% pre-stretched profiles, delamination of the walls was found some places in the quasi-statically tested profile, such as shown in Fig. 20c. Less of this was found in the impacted profiles.

One general conclusion from using the above approach is that there were no profiles completely without fracture. By visual inspection, no fracture was found in the quasi-statically tested 4% pre-stretched profile of AA6063, while cracks were found when studying the CT scans. Also, it seems reasonable to conclude that there is generally more fracture in the impacted profiles than in the quasi-statically tested profiles. Regardless, the main conclusion here is that CT scanning is an excellent tool when studying fracture in complex geometries and it provides the possibility for unlimited slicing of the profiles. The scans will be valuable for validation of future finite element simulations.

6. Discussion

There were few clear effects from increasing the impact velocity from 8 m/s up to 12 m/s. The deformation pattern of the profiles within each test series varied notably, but the corresponding variation in energy absorption was small. As the range of impact velocities was small, the effect was expected to be limited. The deformation mode of the first fold was, however, seen to change when going from an impact velocity of 10 m/s to 12 m/s. Using previously established terminology for crushing modes in square profiles [30], at 12 m/s one of the two chambers folded in an extensional deformation mode rather than the symmetric mode that was seen at the other velocities. Although the extensional deformation mode is reported to dissipate more energy than the symmetric deformation mode in thin-walled square profiles [3,30], there was no evident effect on the overall energy absorption in the current study from this change in deformation mode. However, the mean force curves in Fig. 16 indicate that there could be an effect, as the 12 m/s-tests in three out of the four materials have a higher mean force after the initial peak than the tests performed at the other impact velocities. As the deformation progresses, the mean force levels out for the tests performed at the different velocities. It is noted that no repetitions were performed for the four alloy–pre-stretch combinations at each impact velocity, and a certain statistical scatter is to be expected in the dynamic tests, despite the excellent repeatability reported in the quasi-static tests. Together with the small differences, the lack of repetitions precludes drawing firm conclusions on the effect of the impact velocity, but it is clear that the differences are small within the range of velocities applied here.
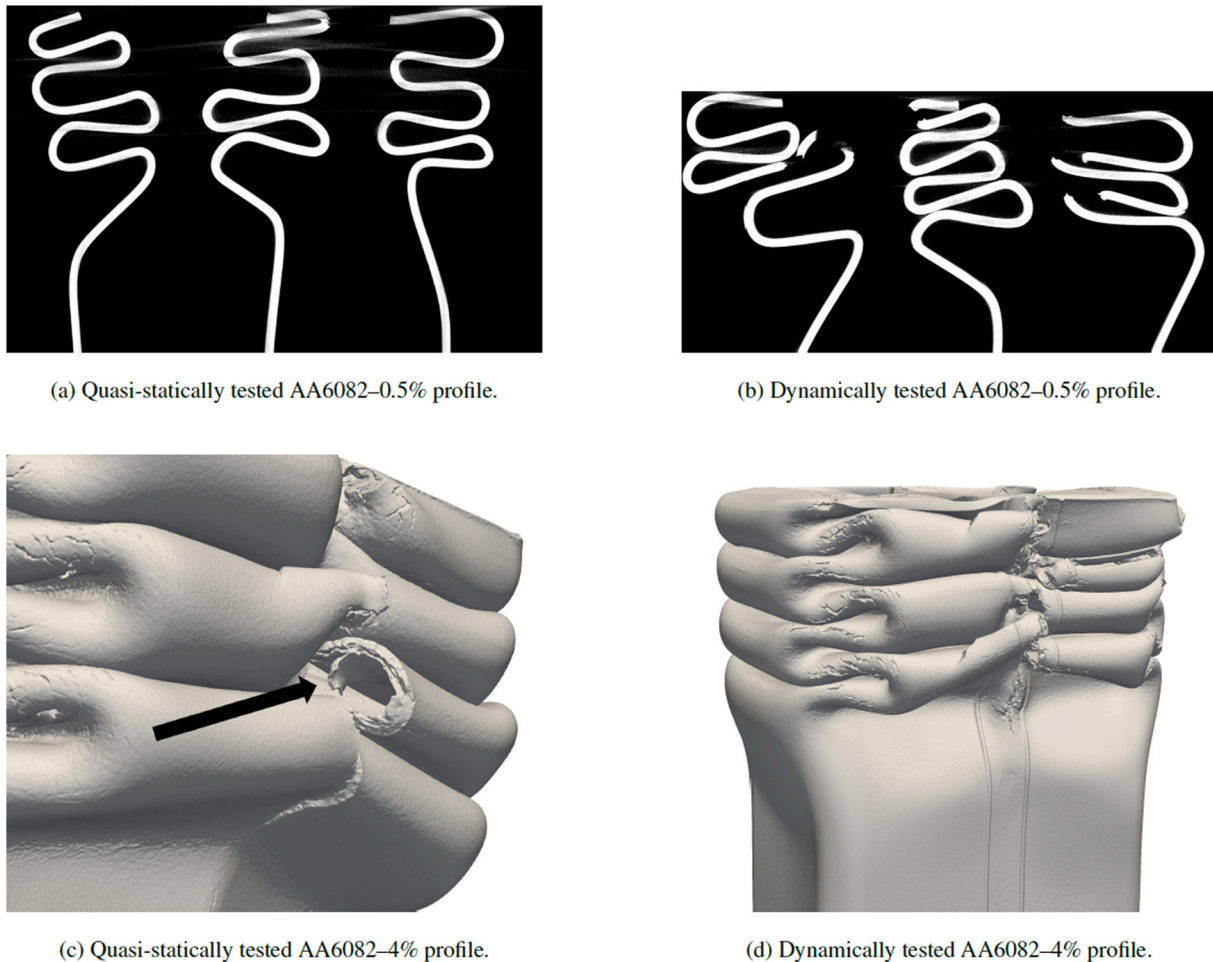
The two alloys in this study responded differently to pre-stretching in terms of yield strength. The yield strength of AA6063 decreased, while the yield strength of AA6082 increased, when extruded profiles were stretched 4% opposed to only 0.5% before artificial ageing. The ultimate tensile strength of the alloys was in both cases reduced with higher pre-stretch. Pre-stretching will increase the strength contribution from

(a) Quasi-statically tested AA6063–0.5% profile.

(b) Dynamically tested AA6063–0.5% profile.

(c) Quasi-statically tested AA6063–4% profile.

(d) Dynamically tested AA6063–4% profile.

Fig. 19. Surface renderings of the CT scans showing fracture in the AA6063-profiles. Arrows accentuate some places where fracture can be seen. (a) shows the T-junction of the quasi-statically tested AA6063–0.5%-profile. The view is close to parallel to the outer wall and onto the inner wall, and fracture is most evident on the inner wall at the lower few folds. (b) shows the T-junction of the impacted AA6063–0.5%-profile, parallel to the inner wall and onto the interior surface of the outer walls, where fracture is seen. (c) shows the corner of the quasi-statically tested AA6063–4%-profile, where a small crack is located between the lower two folds of the side wall on the right side. (d) shows the T-junction of the impacted AA6063–4%-profile. The view is onto the exterior surface of the outer wall, where the folds are fractured at the transition between the inner and outer walls.

dislocations, as the dislocation density is increased, while the strength contribution from precipitates is reduced by pre-stretching due to the coarsening of the precipitate structure. Hence, it is reasonable that different alloys can experience either a net increase or a net decrease in strength by pre-stretching, and many factors in the processing of the materials can become important. One factor that should be kept in mind is that the differently pre-stretched profiles of each alloy were artificially aged for the same time. As found in the TEM-study, and reported in the literature [15–17], pre-stretching results in accelerated overageing and thus different ageing times to peak strength. Hence, the pre-stretched profiles could potentially be at different stages in ageing, e.g., one of them at peak, while the other was overaged or underaged. Other factors that could be significant are the duration of the intervals between extrusion and stretching and between stretching and artificial ageing,

and the heating rate to the ageing temperature. The effect of pre-stretching on the ductility is, to the authors' knowledge, not addressed in the literature. The pre-stretching was here seen to increase the ductility for both alloys. This could be a result of the activation of more slip systems in the material and/or a sub-grain/cell structure in the material where the dislocations at the cell boundaries are locked by the precipitates formed at the dislocation network, which makes the cell boundaries and the softer internal cell structure act as a dislocation source upon further deformation. Thus, this will likely spread the deformation more than in a material without this cell structure. For AA6063, pre-stretching resulted in a higher increase in tensile ductility than for AA6082. TEM showed that the dislocation cell structure was more prominent in AA6063 than in AA6082, which could have had an influence on this finding. The TEM study also indicated that the

(a) Quasi-statically tested AA6082–0.5% profile.

(b) Dynamically tested AA6082–0.5% profile.

(c) Quasi-statically tested AA6082–4% profile.

(d) Dynamically tested AA6082–4% profile.

Fig. 20. 2D slices and surface renderings of the CT-scanned AA6082-profiles. (a) and (b) are 2D slices from ImageJ in the plane parallel to the flanges, while (c) and (d) are surface renderings from ParaView. (a) shows a slice of the inner and side walls of the quasi-statically tested AA6082–0.5%-profile, where some cracks can be found, but no through-the-wall fracture. (b) shows the impacted AA6082–0.5%–profile, where the folds are clearly fractured. (c) shows the quasi-statically tested AA6082–4%–profile, with the arrow pointing to an example of the delamination fracture mode. (d) shows the impacted AA6082–4%–profile. There is extensive cracking in the corners and fracture at the T-junction, as well as fracturing along the folds.

formation of the cell structure is enhanced by low overall precipitate number density with a high portion of the precipitates on the dislocation lines. The reduction in precipitate number density from 0.5% pre-stretch to 4% pre-stretch is similar in the two alloys, while the ratio of precipitates nucleated on dislocation lines to the overall precipitate number density in the 4% pre-stretched materials is much higher for AA6063 than for AA6082.

The T-junctions of the profiles were typical locations for fracture to occur, and the general amount of fracture in the profiles was increased in the dynamic tests compared to the quasi-static tests. These two observations correspond with previous studies on double-chamber profiles [9, 12]. Certain modes of fracture of the T-junction were associated with a change in deformation from mode A to mode B, see Fig. 14. While in mode A the corners and the T-junctions are kept perpendicular, the mode B folding is understood to excessively strain these zones, causing material failure. The mode A folding was also associated with a more steady energy absorption than the mode B folding, which is also preferable for a crash box. However, the tendency for the change in deformation mode was reduced in the dynamic tests, hence the most severe fracture modes of the T-junction are less relevant in the actual application of such a profile.

AA6082 was clearly less ductile than AA6063, as observed in both the crushing tests and the tensile tests and quantified by 2D-DIC on the tensile tests. It is not possible to extract exactly how much the energy

absorption is affected by the ductility from the tests, but some observations can be made. Despite a high increase in ductility for AA6063 with increased pre-stretch, the increase in ductility did not result in higher energy absorption of the 4% pre-stretched profiles. This finding implies that the fracture in the 0.5% pre-stretched profiles did not reduce the energy absorption significantly and was compensated by the higher strength. In contrast, the increased ductility of AA6082 with the higher pre-stretch seemed to have a positive effect on the energy absorption of the profiles. As the yield strength of the 4% pre-stretched AA6082 alloy is slightly higher than that of the 0.5% pre-stretched alloy, while the ultimate tensile strength is slightly lower, a moderate difference in energy absorption could be assumed for these two materials in a case with no fracture. Although there were notable differences in the amount of fracture in the quasi-static tests, the difference in energy absorption was small, suggesting that the effect of fracture on the energy absorption was limited. However, going from quasi-static to dynamic loading, the amount of fracture in the 0.5% pre-stretched AA6082-profiles increased markedly more than in the profiles of the other materials. The corresponding average increase in energy absorption from quasi-static to dynamic loading was lower for the 0.5% pre-stretched AA6082-profiles than for the other materials. Thus, the higher ductility of the 4% pre-stretched profiles seemed to improve the energy absorption. Despite the positive effect from the increased ductility, the tests also show that the amount of fracture that can occur

before it has a significant impact on the energy absorption is rather large, considering the amount of fracture in the dynamically tested 0.5% pre-stretched profiles and the relatively small reduction in energy absorption compared to the 4% pre-stretched profiles.

7. Concluding remarks

In this study, double-chamber aluminium alloy profiles were crushed quasi-statically and dynamically. The profiles were pre-stretched to two different levels of plastic strain, 0.5% and 4%, before being artificially aged to temper T6. The yield strength of the two alloys was affected differently by the pre-stretching, as it decreased for AA6063 while it increased for AA6082. The ultimate tensile strength decreased for both alloys. The higher level of pre-stretch resulted in higher ductility, both in terms of increased tensile ductility, as well as reduced amount of fracture in the crushed profiles. The tensile ductility was found using 2D-DIC, and showed that it is important to consider the local strain rather than the global elongation at fracture as a ductility measure, as these measures displayed entirely different trends amongst the materials. By TEM, it was found that the increased ductility with pre-stretch could be caused by an enhancement of the formation of dislocation cells during further deformation after pre-stretching and ageing. This would also correspond with the higher increase in tensile ductility with pre-stretch seen for AA6063 than for AA6082. In the crushing tests, the higher level of pre-stretch resulted in decreased energy absorption for AA6063, while the energy absorption on average increased for AA6082. CT scans were used to assess fracture in the profiles more thoroughly than what would be possible by visual inspection, even by cutting the profiles. It was observed that fracture and deformation modes are closely coupled, as some deformation modes cause certain fracture modes, and fracture affects the following deformation. In accord with previous studies, quasi-static and dynamic loading caused different deformation and fracture modes, and dynamic loading generally increased the amount of fracture. Compared to quasi-static loading, dynamic loading also caused an increased energy absorption by on average 15%, in addition to an increased peak force.

Credit author contribution statement

Kristin Qvale: Formal analysis, Investigation, Writing - original draft, Writing - review & editing, Visualization. **Odd Sture Hopperstad**: Conceptualization, Writing - review & editing, Supervision, Funding acquisition. **Oddvin Reiso**: Conceptualization, Resources, Writing - review & editing. **Ulf Håkon Tundal**: Conceptualization, Resources, Writing - review & editing. **Calin Daniel Marioara**: TEM study: Formal analysis, Investigation, Writing - original draft, Visualization. **Tore Børvik**: Conceptualization, Writing - review &editing, Supervision, Funding acquisition.

Declaration of competing interest

The authors declare that they have no known competing financial interests or personal relationships that could have appeared to influence the work reported in this paper.

Acknowledgements

References

[1] D. Al Galib, A. Limam, A. Combescure, Influence of damage on the prediction of axial crushing behavior of thin-walled aluminum extruded tubes, Int. J. Crashworthiness 11 (1) (2006) 1–12, https://doi.org/10.1533/ijcr.2005.0379.

[2] G. Gu, Y. Xia, Q. Zhou, On the fracture possibility of thin-walled tubes under axial crushing, Thin-Walled Struct. 55 (2012) 85–95, https://doi.org/10.1016/j.tws.2012.03.005.

[3] M. Langseth, O.S. Hopperstad, Static and dynamic axial crushing of square thin-walled aluminium extrusions, Int. J. Impact Eng. 18 (7–8) (1996) 949–968.

[4] H. Granum, O.R. Myhr, T. Børvik, O.S. Hopperstad, Nanostructure-based finite element analyses of aluminium profiles subjected to quasi-static axial crushing, Thin-Walled Struct. 131 (2018) 769–781, https://doi.org/10.1016/j.tws.2018.07.034.

[5] Y. Chen, A.H. Clausen, O.S. Hopperstad, M. Langseth, Stress-strain behaviour of aluminium alloys at a wide range of strain rates, Int. J. Solid Struct. 46 (21) (2009) 3825–3835, https://doi.org/10.1016/j.ijsolstr.2009.07.013.

[6] D. Karagiozova, M. Alves, Dynamic elastic-plastic buckling of structural elements: A review, Appl. Mech. Rev. 61 (1–6) (2008), https://doi.org/10.1115/1.2939481, 040803–1–040803–26.

[7] X.W. Zhang, H. Su, T.X. Yu, Energy absorption of an axially crushed square tube with a buckling initiator, Int. J. Impact Eng. 36 (3) (2009) 402–417, https://doi.org/10.1016/j.ijimpeng.2008.02.002.

[8] H.G. Fjær, B.I. Bjørneklett, O.R. Myhr, Microstructure based modelling of Al-Mg-Si alloys in development of local heating processes for automotive structures, in: MPMD Sixth Global Innovations Proceedings - Trends in Materials and Manufacturing Technologies for Transportation Industries and Powder Metall, Research and Development in the Transportation Industry, 2005, pp. 95–100.

[9] M. Costas, D. Morin, O.S. Hopperstad, T. Børvik, M. Langseth, A through-thickness damage regularisation scheme for shell elements subjected to severe bending and membrane deformations, J. Mech. Phys. Solid. 123 (2019) 190–206, https://doi.org/10.1016/j.jmps.2018.08.002.

[10] W. Chen, T. Wierzbicki, Relative merits of single-cell, multi-cell and foam-filled thin-walled structures in energy absorption, Thin-Walled Struct. 39 (4) (2001) 287–306, https://doi.org/10.1016/S0263-8231(01)00006-4.

[11] X. Zhang, G. Cheng, H. Zhang, Theoretical prediction and numerical simulation of multi-cell square thin-walled structures, Thin-Walled Struct. 44 (11) (2006) 1185–1191, https://doi.org/10.1016/j.tws.2006.09.002.

[12] H. Hooputra, H. Gese, H. Dell, H. Werner, A comprehensive failure model for crashworthiness simulation of aluminium extrusions, Int. J. Crashworthiness 9 (5) (2004) 449–464, https://doi.org/10.1533/ijcr.2004.0289.

[13] X. Zhang, Z. Wen, H. Zhang, Axial crushing and optimal design of square tubes with graded thickness, Thin-Walled Struct. 84 (2014) 263–274, https://doi.org/10.1016/j.tws.2014.07.004.

[14] G.E. Totten, D.S. MacKenzie, Handbook of Aluminum, in: Physical Metallurgy and Processes, vol. 1, Marcel Dekker, Inc., 2003.

[15] K. Teichmann, C.D. Marioara, S.J. Andersen, K. Marthinsen, The effect of preaging deformation on the precipitation behavior of an Al-Mg-Si alloy, Metall. Mater. Trans. A: Phys. Metall. Mater. Sci. 43 (11) (2012) 4006–4014, https://doi.org/10.1007/s11661-012-1235-0.

[16] M. Kolar, K.O. Pedersen, S. Gulbrandsen-Dahl, K. Teichmann, K. Marthinsen, Effect of pre-deformation on mechanical response of an artificially aged Al-Mg-Si alloy, Mater. Trans. 52 (7) (2011) 1356–1362, https://doi.org/10.2320/matertrans.L-MZ201127.

[17] T. Furu, O. Ryen, O.R. Myhr, Effect of pre-deformation on age hardening kinetics in commercial 6xxx alloys, in: Proc. 11th Intern. Conf. Aluminium Alloys, 2008, pp. 1626–1633.

[18] J.E. Hatch, Aluminum: Properties and Physical Metallurgy, fourth ed., American Society for Metals, 1984.

[19] N.-H. Hoang, O.S. Hopperstad, O.R. Myhr, C. Marioara, M. Langseth, An improved nano-scale material model applied in axial-crushing analyses of square hollow section aluminium profiles, Thin-Walled Struct. 92 (2015) 93–103, https://doi.org/10.1016/j.tws.2015.02.013.

[20] E. Fagerholt, eCorr v4.0 Documentation. http://folk.ntnu.no/egilf/ecorr/doc/, 2017. (Accessed 12 October 2019).

[21] I.J. Polmear, Light Alloys: From Traditional Alloys to Nanocrystals, fourth ed., Butterworth-Heinemann, 2006.

[22] M. Khadyko, D. Morin, T. Børvik, O.S. Hopperstad, Tensile ductility of extruded aluminium alloy AA6063 in different tempers, Mater. Sci. Eng. A 744 (2019) 500–511, https://doi.org/10.1016/j.msea.2018.12.048.

[23] G.E. Dieter, Mechanical Metallurgy, SI Metric Edition, McGraw-Hill Book Co, 1988.

[24] C.D. Marioara, S.J. Andersen, H.W. Zandbergen, R. Holmestad, The influence of alloy composition on precipitates of the Al-Mg-Si system, Metall. Mater. Trans. A: Phys. Metall. Mater. Sci. 36 (13) (2005) 691–702, https://doi.org/10.1007/s11661-005-0185-1.

[25] N.-H. Hoang, M. Langseth, G. Gruben, T. Coudert, Behaviour of two chamber aluminium profiles under axial crushing: an experimental and numerical study, in: ACOME 2017: Proceedings of the International Conference on Advances in Computational Mechanics 2017, 2018, pp. 657–672, https://doi.org/10.1007/978-981-10-7149-2_45.

[26] A.G. Hanssen, T. Auestad, T. Tryland, M. Langseth, The kicking machine: A device for impact testing of structural components, Int. J. Crashworthiness 8 (4) (2003) 385–392, https://doi.org/10.1533/ijcr.2003.0246.

[27] D. Morin, B.L. Kaarstad, B. Skajaa, O.S. Hopperstad, M. Langseth, Testing and modelling of stiffened aluminium panels subjected to quasi-static and low-velocity

impact loading, Int. J. Impact Eng. 110 (2017) 97–111, https://doi.org/10.1016/j.ijimpeng.2017.03.002.

[28] National Institutes of Health, ImageJ: Image processing and analysis in Java. https://imagej.nih.gov/ij/, 2019. (Accessed 10 December 2019).

[29] ParaView. https://www.paraview.org/, 2019. (Accessed 10 December 2019).

[30] W. Abramowicz, N. Jones, Dynamic progressive buckling of circular and square tubes, Int. J. Impact Eng. 4 (4) (1986) 243–270, https://doi.org/10.1016/0734-743X(86)90017-5.